Dark Current Modeling and Characterization of Amorphous Lead Oxide-Based X-ray Photoconductive Devices for Applications in Medical Imaging

By

Tristen Thibault

A thesis

Presented to Lakehead University

In partial fulfillment of the

requirement for the degree of

Master of Science in Physics

Thunder Bay, Ontario, Canada, 2022

© Tristen Thibault 2022

Abstract

High atomic number (Z) polycrystalline and amorphous photoconductors are currently being investigated to extend direct conversion X-ray detectors to real-time and high-energy low-dose applications. Amorphous lead oxide (a-PbO) is one of the most promising photoconductor candidates because of its negligible signal lag and high theoretical X-ray conversion efficiency. However, a-PbO layers are still experimental; PbO technology has been developed to the point where material science and engineering approaches must be applied to make a-PbO detector prototypes suitable for low-dose X-ray imaging. This includes determining the most appropriate a-PbO multilayer detector structures with specially designed blocking layers that will withstand the high electric fields needed for efficient (i.e., complete) collection of X-ray generated charge while maintaining an acceptable dark current (DC) level. DC is a source of noise in the detector structure that degrades the signal-to-noise ratio (SNR) of the detector system in low-exposure applications. Here we investigate the use of polyimide (PI) as a hole-blocking layer. PI blocking layers were proven successful in the only commercially used direct conversion detectors, which are based on layers of photoconductive amorphous selenium (a-Se). Experimentally, PI was shown to have the most suitable electrical and physical properties for our a-PbO technology. In addition, PI has a straightforward application process of spin coating. Therefore, PI was chosen as a hole blocking layer to decrease DC to tolerable levels in an a-PbO-based detector.

X-ray-induced photocurrent method (XPM), performed in pulsed and continuous variations, confirmed that the inclusion of a thin PI layer in the detector structure does not degrade the performance of the a-PbO-based detector: when an electrical field of 20 V/μm (a typical operational applied bias for direct conversion detectors) is applied to a PI/a-PbO detector prototype and it is exposed to a beam of X-rays modulated at 30 Hz (a conventional frame rate used in

fluoroscopy), the signal lag remains at a level of ~1%, which is appropriate for real-time (dynamic) applications. Another focus of this work is to investigate the DC behaviour of the detector structure at different applied electric fields relevant to the practical operation of direct conversion detectors (5, 10, 15, and 20 V/μm). A theoretical model was derived to simulate the experimental results of the transient DC behaviour exhibited by a PI/a-PbO detector. The model follows the concept which was developed to simulate the transient DC behaviour observed in *n-i-p, n-i,* and PI/a-Se detectors. However, it is extended to account for the particularities of a-PbO while incorporating charge transport and trapping mechanisms that are theoretically and experimentally supported by the behaviour of disordered inorganic and organic semiconductors. Although the model uses a simplified representation of the energetic disorder in the PI layer, a good agreement between simulated and experimental DC kinetics is observed. The model suggests that, immediately after the bias application, DC is primarily controlled by the injection of holes from the positively biased ITO electrode before gradually decreasing to a steady-state value governed by thermal excitation and subsequent multiple-trapping (MT) controlled transport of holes within the a-PbO layer. DC decays via the accumulation of holes trapped in deep localized states in the PI layer, which screens the electric field at the ITO/PI interface, redistributing it throughout the detector, and decreasing injection. The developed model considers the recently proposed theory that field-induced carrier release from deep traps into the extended states can be enhanced by hopping transitions of carriers between localized states within the mobility gap. The incorporation of a hopping-enhanced de-trapping process allows for better agreement between experimental and simulated data thus validating the theory of the hopping-assisted release of charge carriers from deep traps.

The proposed model can be used to optimize the design of PI/a-PbO detectors, i.e., to estimate the optimal PI blocking layer thickness for the required operational bias and a-PbO layer

thickness. Additionally, it allows one to estimate the increase of the internal electric field inside the a-PbO layer, which is a result of the electric field redistribution. This has the benefit of improving charge collection efficiency and temporal performance over time, as confirmed by experimental results.

Acknowledgments

I would like to thank my supervisor, Dr. Alla Reznik, for guiding and encouraging me through my graduate degree. Our discussions together pertaining to my Masters' research were unbelievably valuable and often encouraged me to dive deeper into the physics of charge transport in disordered materials. I would also like to thank Dr. Oleksandr Grynko. Oleksandr is the lead researcher of the lead oxide group, and as such, we worked very closely together. Oleksandr and I collaborated on virtually every aspect of my graduate degree. I would also like to thank my supervisory committee, Dr. Linhananta and Dr. Gallagher.

In addition, I extend my gratitude to everyone (past and present) that worked as a part of Reznik's group of advanced detection devices. The sense of community and collaboration at the research lab aided greatly in my enjoyment of my degree. Lastly, I would like to thank my family and soon-to-be wife, Jade Ross, for their support.

Table of Contents

Abstract ii

Acknowledgments iv

Table of Contents v

List of Figures vii

List of Acronyms x

Chapter 1: Introduction 1

1.1 X-ray Imaging 1

1.2 Indirect Conversion Detection 3

1.3 Direct Conversion Detection 5

1.4 Disordered Photoconductors for Direct Conversion Detectors 7

1.3.1 Density of States and Charge Transport 11

1.5 Dark Current (DC) 15

1.5.1 Thermal Excitation 17

1.5.2 Injection 19

1.6 Blocking Layers to Suppress DC 24

1.6.1 Doped/Alloyed a-Se (p-like and n-like) 26

1.6.2 Oxides (TiO_2 and CeO_2) 28

1.6.3 Sb_2S_3 29

1.6.4 Polymers (PI and PTCBI) 30

1.7 PI/a-PbO Detectors 31

Chapter 2: Dark Current Modeling for a Polyimide – Amorphous Lead Oxide-based Direct Conversion X-ray Detector 33

2.2 Materials and Methods 37

2.2.1 Detector Fabrication 37

2.2.2 Experimental Setup – Temporal Performance and Sensitivity Characterization 38

2.2.3 Experimental Setup - DC kinetics 40

2.3 Results 41

2.3.1 Temporal Performance and Sensitivity Characterization 41

2.3.2 DC Kinetics 43

2.3.3 Mathematical Model 44

2.4 Discussion 53

2.5 Conclusions 63

Chapter 3: Conclusions 66

3.1 PI/a-PbO Detector Temporal Performance 66

3.2 Dark Current Decay 67

3.2.1 Mechanism of Dark Current Decay 68

3.2.2 Electric Field Redistribution 69

3.3 Future Work and its Significance 69

Appendix A. Lag Calculations 70

Appendix B. X-ray Sensitivity Calculations 71

References: 73

List of Figures

Figure 1.1. General scheme of diagnostic X-ray imaging. 2

Figure 1.2. A simplified schematic diagram of a FPXI. 3

Figure 1.3. An indirect conversion X-ray detector where a scintillator or phosphor layer is coupled to a PD array in conjunction with a TFT array. The absorption of an X-ray generates optical light, which is then detected by the PD array and created charge is collected in the TFT array. 4

Figure 1.4. A schematic of a direct conversion X-ray detector where a photoconductor layer is coupled with a TFT imaging array. An X-ray is absorbed in the photoconductor layer creating EHP that drift towards the electrodes under the influence of an applied field. 6

Figure 1.5. (a) The SEM (Scanning Electron Microscopy) cross-sectional view of the poly-PbO. The inset to the figure shows the surface of the poly-PbO layer. (b) SEM cross-sectional view of the a-PbO. The inset to the figure shows the surface of the a-PbO layer. 10

Figure 1.6. The density of states (DOS) plotted as a function of energy for a typical disordered semiconductor. Here localised states form band tails. 12

Figure 1.7. An illustration of the multiple trapping (MT) transport process. The magnified portion displays field-assisted tunneling that lowers the activation energy to escape from a localised state. 14

Figure 1.8. The band-energy diagram of a disordered photoconductor with a peak in the DOS within the mobility gap, resulting from defect states. Here, thermal excitation can occur from an interband transition or from the defect states with a DOS. 18

Figure 1.9. The formation of a Schottky barrier upon physical connection of a metal and a semiconductor. Here $E_{F,S} > E_{F,M}$, and as a result the band structure of the semiconductor bends up at the interface. 20

Figure 1.10. The potential on an electron near the surface of a negatively biased metal in a vacuum. The application of a negative bias lowers the barrier height an electron must overcome to escape the metal by a factor of $e\Delta\Phi$. The barrier is lowered by the interaction of the image lowering energy and the potential energy of the field. 22

Figure 1.11. Energy-band diagram for a metal interfaced with an n-type semiconductor under different applied fields. F > 0 refers to a field that points from semiconductor to the metal (right to left). $F_1 > 0$ lowers $e\Phi_{B,Therm}$ by $\beta_S F1$ and $F_2 < 0$ increases $e\Phi_{B,Therm}$ by $\beta_S F2$. 23

Figure 1.12. An illustration of a detector with both an electron and hole blocking layers present in its structure. The blocking layers here prevent the injection of one species of charge while allowing photogenerated charge of the opposite polarity to pass. 25

Figure 1.13. An energy level schematic of a) FTO interfaced with TiO_2 and b) ITO interfaced with CeO_2. 28

Figure 1.14. The spin coating process used to deposit PI. A controlled amount of PI is dropped onto a substrate, the substrate is the spun at a high rpm that causes the PI to evenly spread out into a uniform layer, and then the substate is heated to evaporate the solvents, curing the PI. 30

Figure 1.15. A prototype direct conversion detector that utilizes a-PbO as an X-ray–to–charge transducer and a PI hole blocking layer (not to scale). 32

Figure 2.1 a) Schematic diagram (not to scale) and b) a cross-sectional scanning electron microscopy (SEM) image of a single-pixel PI/a-PbO direct conversion X-ray detector. 38

Figure 2.2. Experimental setups for a) modulated and continuous XPM and b) DC kinetics. 39

Figure 2.3. The X-ray response of the PI/a-PbO detector, biased at 20 V/μm, to a continuous (black) and modulated (red) beam of X-rays. Modulated beam has a frame rate of 30 frames per second, matching that used in fluoroscopy. The photocurrent is normalized to the steady-state magnitude of the continuous response. 42

Figure 2.4. The ratios of $W_{\pm}$ measured immediately after the application of the bias ($W \pm inst.$) to $W_{\pm}$ measured after waiting 10 minutes post bias application ($W \pm inst. W \pm$). Note that W±, measured 10 minutes after the bias was applied, was chosen as the reference point because it is observed that after this amount of waiting the ehp creation energy remains relatively constant, undergoing very little change over time. 43

Figure 2.5. Experimental DC kinetics data plotted in a semi-log scale corresponding to a PI/a-PbO detector biased at selected fields (5 – 20 V/μm) for two hours. The horizontal dashed line illustrates the operational threshold of 1 pA/mm^2. Data extracted from [27]. 44

Figure 2.6. A simplified schematic diagram of the PI/a-PbO detector and its time-dependent spatial electric displacement field profile. The dashed line represents the displacement field at the instant of bias application. The solid line represents the displacement field profile post-bias application when holes have accumulated in PI. In addition, a schematic of MT transport of thermally generated holes through the bulk of a-PbO is illustrated.. 46

Figure 2.7. Experimental (solid black) and simulated (injected (dash-dotted green), thermal (solid blue), and total (dashed red)) DC kinetics data plotted in a semi-log scale corresponding to a PI/a-PbO detector biased at fields of a) 20 V/μm, b) 15 V/μm, c) 10 V/μm, and d) 5 V/μm for two hours.. 53

Figure 2.8. Electric displacement field (D(t)) at the ITO/PI interface (dashed red) and throughout the bulk of a-PbO (solid black) as functions of time for an applied field of 20 V/μm................ 55

Figure 2.9. Release time ($\tau r, m$) plotted as a function of the instantaneous field at the ITO/PI interface ($FPI(0, t)$). For the deepest level of traps at 1.0 eV ($\tau r, 3$), a stronger field dependence, compared to other levels, yielded a more accurate fit between experimental and simulated data. 58

Figure 2.10. Capture time (τc) as a function of the applied nominal field (F_0). A unique constant τc was given for each applied nominal field to obtain the best fitting between experimental and simulated data. 59

Figure 2.11. Simulated (dashed lines) and experimental (solid lines) DC kinetics data plotted in a semi-log scale corresponding to a PI/a-PbO detector biased at selected fields (5-20 V/µm) for two hours. Here the model is modified by treating the release times ($\tau r, m$) and capture times (τc) as electric field dependent parameters in accordance with the hopping enhanced release and capture mechanisms discussed above. 60

Figure 2.12. The occupancy of trapping sites, segmented into three discrete levels, plotted as a function of time. Here, this data is obtained from the simulated kinetics corresponding to a nominal field of 20 V/µm. Note that this data is simulated from the unmodified model, where hopping assisted release and capture is not accounted for. 61

Figure A.1. The X-ray response of the PI/a-PbO detector to a beam of continuous and modulated beam of X-rays with relevant values indicated for each frame. 71

List of Acronyms

AMA	Active-Matrix Array
CA	Cellulose Acetate
CB	Conduction Band

CELIV	Charge Extraction Through Linearly Increasing Voltage
CMOS	Complementary Metal-oxide Semiconductor
c-Si	Crystalline Silicon
DBT	Digital Breast Tomosynthesis
DC	Dark Current
DOS	Density of States
EHP	Electron-hole Pair
FPXI	Flat Panel X-ray Imager
FTO	Fluorine-doped Tin Oxide
GPIB	General Purpose Interface Bus
HARP	High-gain Avalanche Rushing Photoconductor
HVL	Half Value Layer
ITO	Indium Tin Oxide
MT	Multiple Trapping
NIST	National Institute of Standards and Technology
NSERC	Natural Sciences and Engineering Council of Canada

PD	Photodiode
PI	Polyimide
PTCBI	Perylene Tetracarboxylic Bisbenzimidazole
PVD	Physical Vapour Deposition
SEM	Scanning Electron Microscopy
SNR	Signal to Noise Ratio
TFT	Thin Film Transistor
VB	Valence Band
XPM	X-ray Induced Photocurrent Method
XRII	X-ray Image Intensifiers

Chapter 1: Introduction

1.1 X-ray Imaging

The most widely used clinical application of X-rays in the diagnostic energy range (i.e., from 70 to 140 keV) is in anatomical (or structural) medical imaging. Anatomical medical imaging is a cornerstone of modern medicine and out of all its subsets radiography is the most prevalent method used. For diagnostic procedures, X-rays are generated by an X-ray tube and they either pass through a target (patient) unaffected, as primary or direct radiation, or they are attenuated by the target. As they pass through the target, the beam of X-rays is encoded with information pertaining to the target, primarily tissue density, which is correlated with anatomical structure. This information is encoded by the fluence of the beam (number of photons per unit area) as X-rays will be attenuated more by denser tissue that has larger attenuation coefficients. The role of the detector device is to then 'read' the information carried by the impinging X-ray beam and use it to form a 2-D projection image. The device does this by measuring the incoming X-ray beam's fluence as a function of spatial location. The information of the X-ray beam, and thus the information of the target, are transcribed by the detecting device, and an image can be formed. In Figure 1.1, the general scheme for X-ray imaging is displayed. Currently, the most advanced commercial X-ray detectors are flat-panel X-ray imagers (FPXI) based on solid-state (amorphous silicon, a-Si:H) technology [1].

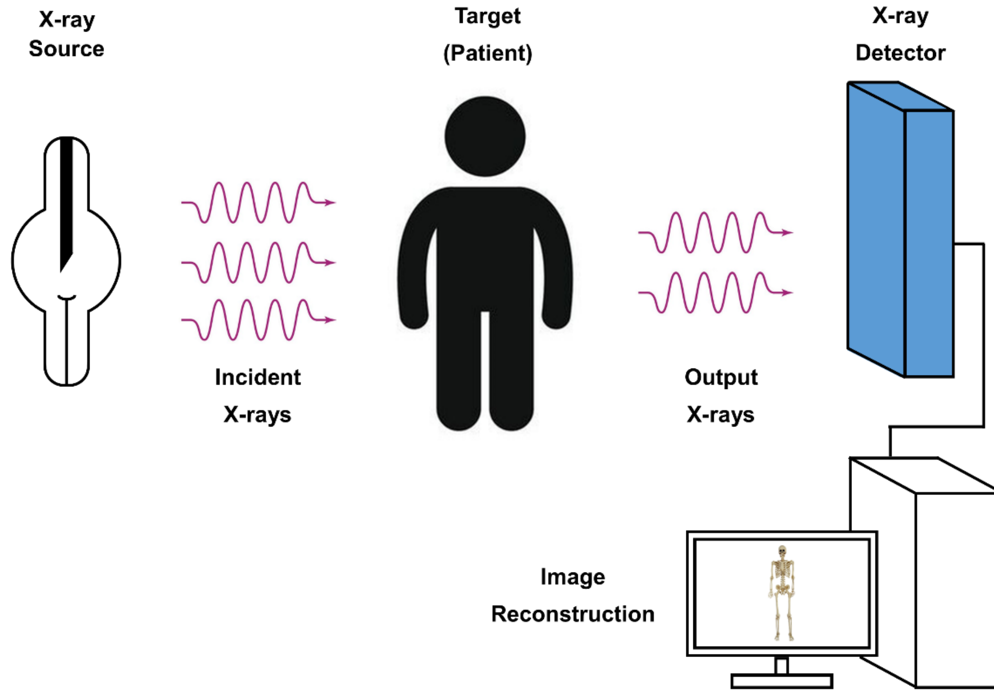

Figure 1.1. *General scheme of diagnostic X-ray imaging.*

FPXIs were made possible by the advent of large-area imaging electronics consisting of an array of a-Si:H thin-film transistors (TFT), first developed for the consumer electronics industry and then adopted by medical imaging. More recently, complementary metal-oxide-semiconductor (CMOS) active-matrix arrays (AMA) have gained popularity, replacing TFT arrays [2], [3]. For the purpose of this thesis, we will focus on TFT array-based FPXI as it is a more widely used technology. A diagram of an FPXI can be seen in Figure 1.2. According to the difference in the pathway of converting X-ray energy to charge carriers, flat-panel X-ray detectors are categorized into indirect conversion systems and direct conversion systems as detailed below.

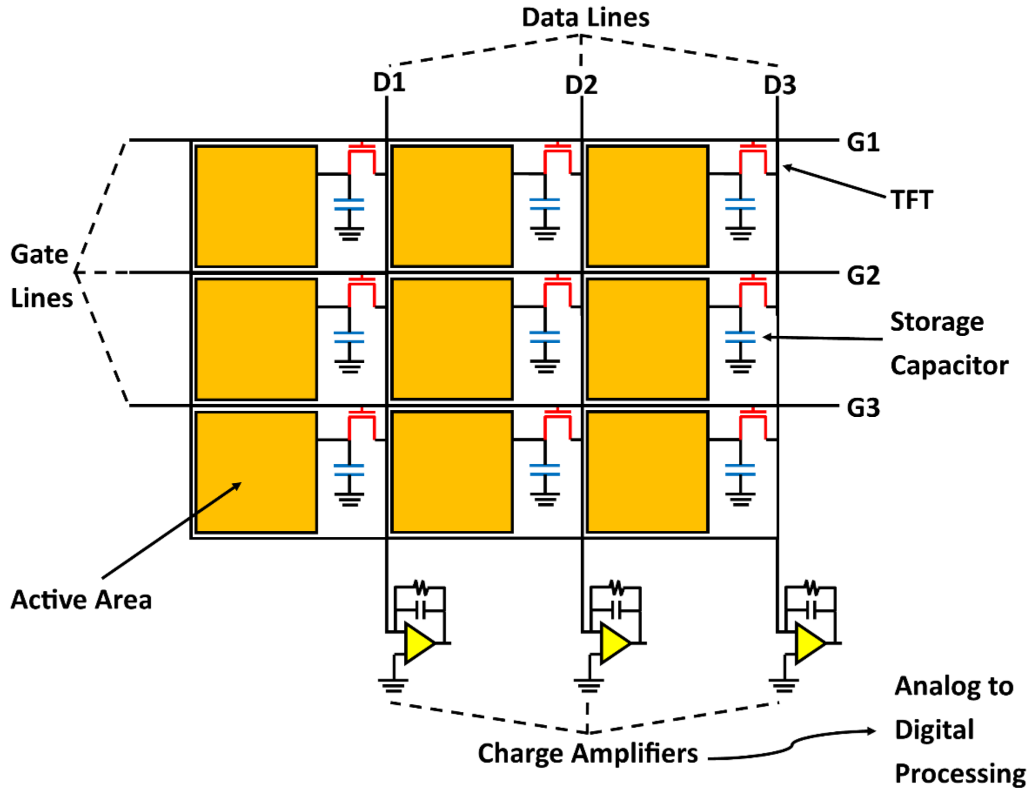

Figure 1.2. *A simplified schematic diagram of a FPXI.*

1.2 Indirect Conversion Detection

Most commercially available FPXIs rely on the indirect conversion of incident X-rays into a signal. Indirect conversion FPXIs utilize a multi-step process to convert incident X-rays into a measurable electric signal. An impinging X-ray photon is initially absorbed by a scintillator (phosphor), which converts X-rays into optical light emitted in every direction. The quantity of emitted optical photons produced by the scintillator is proportional to the energy of the absorbed X-ray. An optically coupled Si photodiode (PD) array detects emitted optical photons and creates an electric signal [4]. The electrical charge created in the photosensor array is then collected by TFT electronics and used to reconstruct an image. Thus, the indirect conversion scheme is named

so because the X-rays are indirectly converted into electrical charge. The indirect conversion detection scheme is seen in Figure 1.3.

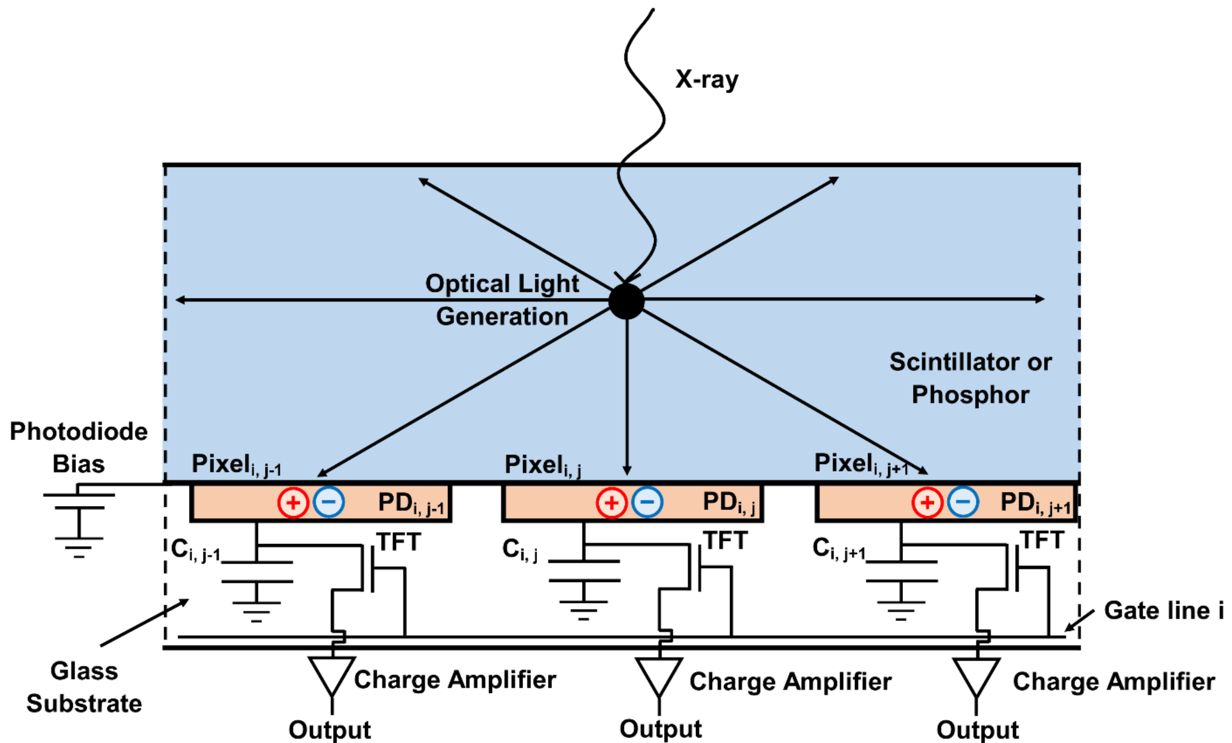

Figure 1.3. *An indirect conversion X-ray detector where a scintillator or phosphor layer is coupled to a PD array in conjunction with a TFT array. The absorption of an X-ray generates optical light, which is then detected by the PD array and created charge is collected in the TFT array.*

The most widely used scintillators are CsI:Tl [4] with a thickness of 150-600 μm and Gd_2O_2S:Tb [4]. The scintillators deposited in indirect flat-panel X-ray detectors can be either unstructured or structured. In unstructured scintillators, such as Gd_2O_2S:Tb powder crystals (turbid phosphors), the emitted light traveling in the materials may spread to the neighboring pixels, creating image blur and reducing spatial resolution. Some portion of optical photons escapes detection altogether by leaving the scintillation material and reducing energy resolution. This

matter could be overcome by utilizing structure scintillators, like CsI:Tl consisting of discrete and parallel 5-10 μm wide fiber-like crystals or 'needles' [5]. Structured CsI:Tl may also utilize optical reflecting boundaries between 'needles' to constrain photons within a given 'needle'. In this case, the luminescence photons only travel along with the 'needles' to the PDs, which improves the spatial resolution and reduces image blur. Even with structured scintillators, the two-stage conversion process creates a secondary quantum sink, causing the X-ray-to-charge conversion gain to be reduced. As a result, CsI:Tl detectors are quantum-limited, meaning that the signal-to-noise ratio (SNR) for a given pixel is proportional to the square root of the number of detected X-rays. Subsequently, at the lowest exposure levels common in fluoroscopy (0.1–1 μR/frame), electronic noise becomes dominant, and the visibility of low-contrast objects is compromised. In fact, at the lowest exposures, CsI:Tl detectors lack the image quality of X-ray image intensifiers (XRII) [2].

1.3 Direct Conversion Detection

The other detection scheme is direct conversion detection. Direct conversion detectors forgo the intermediate step of X-ray conversion to optical light found in the indirect scheme. A thick layer of X-ray-sensitive semiconductive material (photoconductor) is used as an X-ray-to-charge transducer. Upon absorption of X-ray quanta, EHPs are created within the photoconductive layer. A strong (10-15 V/μm) electric field is applied to a photoconductor to prevent mutual recombination of geminate EHPs. The applied electric field guides charge carriers along the field lines to their respective electrodes to be collected. The charge is held within storage capacitors incorporated in a coupled TFT array. The charge stored is read out, amplified, and digitized to reconstruct an image. The typical structure of a direct conversion X-ray detector is illustrated in Figure 1.4.

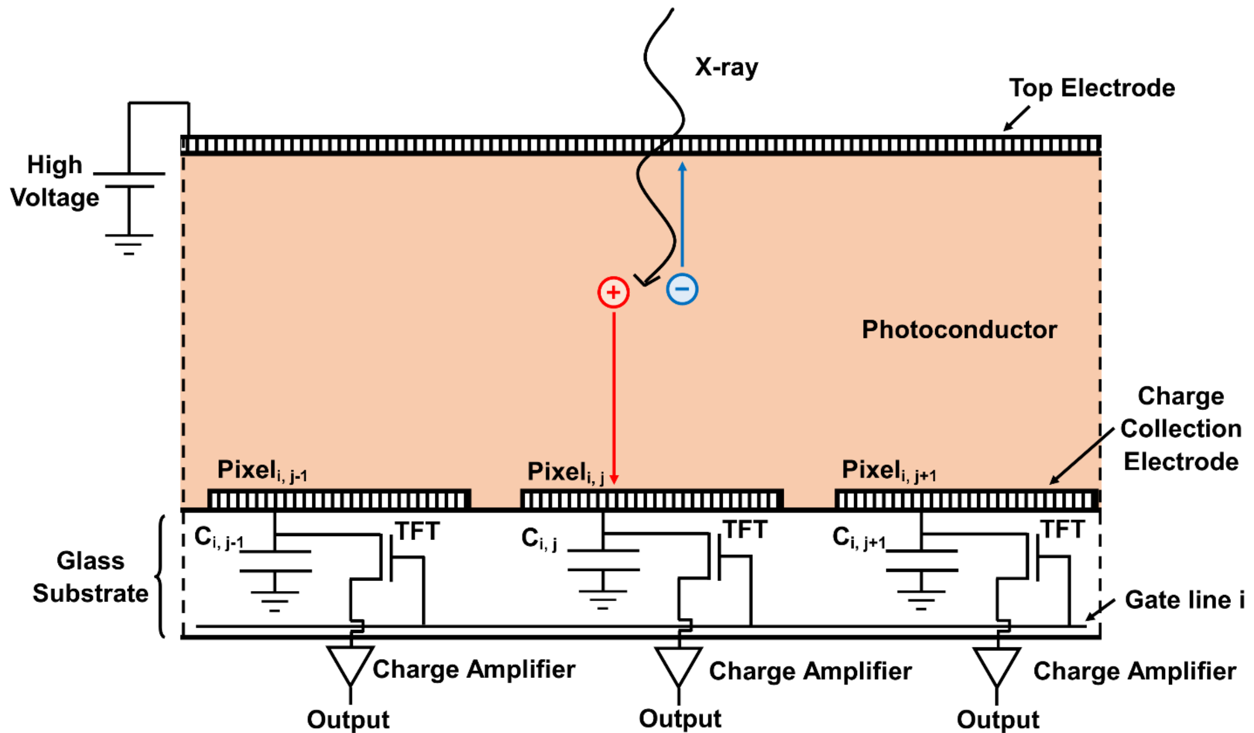

Figure 1.4. *A schematic of a direct conversion X-ray detector where a photoconductor layer is coupled with a TFT imaging array. An X-ray is absorbed in the photoconductor layer creating EHP that drift towards the electrodes under the influence of an applied field.*

Eliminating the intermediate step of optical light generation gives direct conversion detectors inherently better efficiency than indirect conversion detectors. Created charge in the photoconductor layer is guided along field lines to their respective electrodes to be collected, effectively eliminating any lateral spread of the charge carriers. Therefore, direct conversion detectors' spatial resolution is better than indirect conversion detectors [6]. Another benefit inherent to direct conversion is a higher SNR due to the potential for a greater charge generation yield. In addition, the direct conversion system is simpler to manufacture since the need for separately integrated PD is avoided. The performance benefits of direct conversion detectors are actualized if a proper X-ray photoconductor, which acts as an X-ray-to-charge transducer, is used. The ideal photoconductor to be used for a direct conversion detector must meet the following set

of criteria: (1) The material must have a sufficient absorption depth in the energy range of interest to attenuate most of the incident X-rays (> 90-95 %) within a practical detector thickness [6]. This requires a material with a high atomic number (*Z*) and density. (2) The material should have a sufficiently high X-ray sensitivity in terms of X-ray-to-charge conversion gain [6]. This allows the detector to approach quantum noise-limited operation at the lowest exposures specific to a particular application. (3) The dark current (DC) must be low to achieve a desired SNR [6]. DC is a source of noise and will be described in later sections. (4) The material must have a fast temporal response to be feasible for real-time applications such as fluoroscopy. A residual current following an X-ray pulse, known as signal lag, should be less than 5%, i.e., signal lag should be comparable to CsI detectors, which are currently used for fluoroscopic applications [7]. (5) The carrier schubweg (average distance drifted by a carrier before it is deeply trapped or recombines), $s = \mu\tau F$, where μ is charge mobility, τ is the charge lifetime, and *F* is the applied electric field, should be larger than the photoconductor thickness (L) ($s > L$). This condition ensures that the drifting X-ray-generated carriers will not be lost to recombination or trapping before they transit *L* and are collected by electrodes [6]. (6) The deposition process of the photoconductor must be compatible with large-area imaging electronics and be cost-effective [6]. Also, the layer deposition procedure should be well-developed to produce a uniform thickness and be applicable for industrial-scale manufacturing.

1.4 Disordered Photoconductors for Direct Conversion Detectors

The last requirement of the photoconductor being compatible with large-area electronics narrows the potential photoconductor candidates down significantly. The deposition process must be cost-effective. In addition, the deposition process must not heat the substrate above 220-240 °C [8] to not damage the a-Si:H electronics. These requirements eliminate the use of crystalline

photoconductors because their deposition is a high-temperature process, leaving only polycrystalline and amorphous (disordered) materials as suitable photoconductors. Disordered photoconductors are deposited with thermal physical vapour deposition (PVD) that does not heat the substrate above damaging levels [2].

Currently, the only commercially used photoconductor for direct conversion detectors is amorphous selenium (a-Se). a-Se is exclusively used for low-energy imaging such as mammography, where it demonstrates diagnostic capabilities not achievable with indirect conversion detectors [9]–[11]. Unfortunately, a-Se is only suitable at low X-ray energies and high exposures (i.e., for 20 keV energy range used in mammography) while, at the lowest fluoroscopic doses, a-Se direct conversion flat panel detectors suffer from the same problem as CsI indirect ones: they are not quantum-noise limited. Indeed, a-Se direct conversion detectors have approximately the same conversion gain as CsI indirect conversion detectors [4]. Hence, for low-dose fluoroscopic procedures a-Se has to be replaced with high-Z material with high absorption and lower EHP creation energy, thus having higher conversion gain [12].

A lead oxide (PbO) photoconductor is proposed as an alternative to a-Se for direct conversion X-ray detectors for higher energy X-ray applications (including the 120 kVp energy range for chest radiography) and applications that require dynamic or multi-frame imaging (i.e., digital breast tomosynthesis (DBT) performed in 20-30 keV energy range and fluoroscopic applications at 50-70 keV energy range) [7], [12]–[16]. PbO is suitable for high-energy applications due to its higher effective atomic number (Z) and hence higher X-ray detection efficiency than a-Se permitting effective absorption of higher energy X-rays with a thinner layer. As for dynamic and multi-frame applications, an advantage over a-Se is in its lower EHP creation energy, and hence a higher X-ray-to-charge conversion gain. This improves X-ray sensitivity and

allows the creation of high-contrast images at low exposure rates. In addition, the PbO deposition process (thermal PVD) is compatible with flat-panel detector electronics. Philips Research Labs prototyped a PbO-based direct conversion detector with a best-in-class spatial resolution where a thick layer of polycrystalline PbO (poly-PbO) was deposited over a TFT imaging array [17]. However, research at Philips revealed several imperfections of poly-PbO including incomplete charge collection and a signal lag, i.e., a residual current after the termination of an X-ray pulse. The latter was considered as major obstacle to commercialization of poly-PbO layers in direct conversion X-ray detectors. Indeed, the presence of signal lag and subsequently, image lag does not permit the use of poly-PbO detectors in the most clinically demanding area of real-time fluoroscopic imaging.

Previous research revealed the fundamental cause of signal lag in poly-PbO through detailed analyses of its electro-optical and structural properties. An important peculiarity of poly-PbO has been discovered: in contrast to other disordered materials (i.e., inorganic amorphous and polycrystalline solids and organic polymers), poly-PbO does not contain energetically distributed localized states in its band tails; as such, the transport of X-ray generated charge carriers is governed by the spatial inhomogeneity of the material rather than energy disorder. Poly-PbO layers are highly porous and consist of randomly oriented platelets several microns in diameter and a few hundred nanometers thick as seen in Figure 1.5a. Platelet-related spatial disorder creates spatially distributed monoenergetic localized states with very long release times [18]. Trapped carriers cannot leave these states since the absence of energy disorder restricts random walk. Long release times lead to very dispersive carrier transport and signal lag.

These findings suggested a new direction towards the optimization of PbO technology that was targeted to suppress structural inhomogeneity in such a way as to combat the formation of

individual platelets and to promote the growth of a highly packed homogeneously disordered material. With this goal, PbO deposition technology was advanced to produce a novel type of glassy, or amorphous lead oxide (a-PbO). By developing and applying an ion-enhanced physical vapor deposition (PVD) technique [19], uniform and void-free a-PbO layers, without a platelet structure typical of poly-PbO, were obtained, displayed in Figure 1.5b. As is shown in the inset of Figure 1.5b, the absence of platelets results in a smooth surface of the grown layer, never achieved before with polycrystalline films. In comparison with its polycrystalline counterpart, a-PbO is non-hydroscopic, stable in air, and has lower DC at higher electric fields compared to poly-PbO. Performance evaluation has shown that the signal lag is suppressed to a level that is suitable for fluoroscopic applications. Indeed, measured X-ray responses show almost complete elimination of signal lag to the level sufficient for high-speed operations [7], [13], [16].

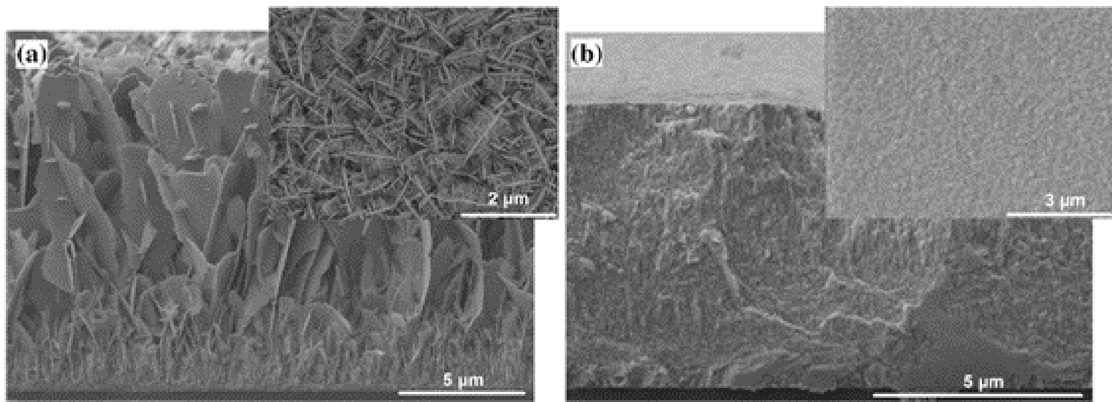

Figure 1.5. *(a) The SEM (Scanning Electron Microscopy) cross-sectional view of the poly-PbO. The inset to the figure shows the surface of the poly-PbO layer. (b) SEM cross-sectional view of the a-PbO. The inset to the figure shows the surface of the a-PbO layer.*

It should be noted that while the elimination of signal lag represents a breakthrough in PbO technology, there is still much research needed for the improvement of the technology and to enhance the properties of a-PbO as an X-ray-to-charge transducer. There are many aspects of X-

ray photoconductor and detector fabrication that are not fully understood or simply not known. One of the few shortcomings that a-PbO must overcome is that it exhibits higher than tolerable DC levels.

1.3.1 Density of States and Charge Transport

To implement a solution to suppress DC, it is important to first understand the origin of DC. Disordered semiconductors, such as a-PbO, are characterized by their low drift mobilities compared with crystalline materials. Low mobility in amorphous materials is strongly connected with the disorder-induced localized states that extend from the conduction band (CB) and valence band (VB) into what is the bandgap in the case of its ideal single-crystal counterpart. Due to the absence of traditional band edges, the electronic properties of disordered semiconductors are explained with an equivalent concept of 'mobility edges' separating extended and localized states [20]. Extended states are spatially close enough that the wave function of a charge carrier in those states extends through the entire volume of the material and can move freely [21]. Localized states are spatially sparse enough that a charge carrier in these states will possess a localized wave function [21]. The energies at which the transitions between extended and localized states occur are labeled as mobility edges (valence mobility edge (E_v) and conduction mobility edge (E_c)). The energy difference between E_c and E_v is the mobility gap (E_g). The mobility gap and its distribution of the density of states (DOS) are some of the most fundamental characteristics of disordered semiconductors. A typical band-energy diagram for a disordered photoconductor is seen in Figure 1.6.

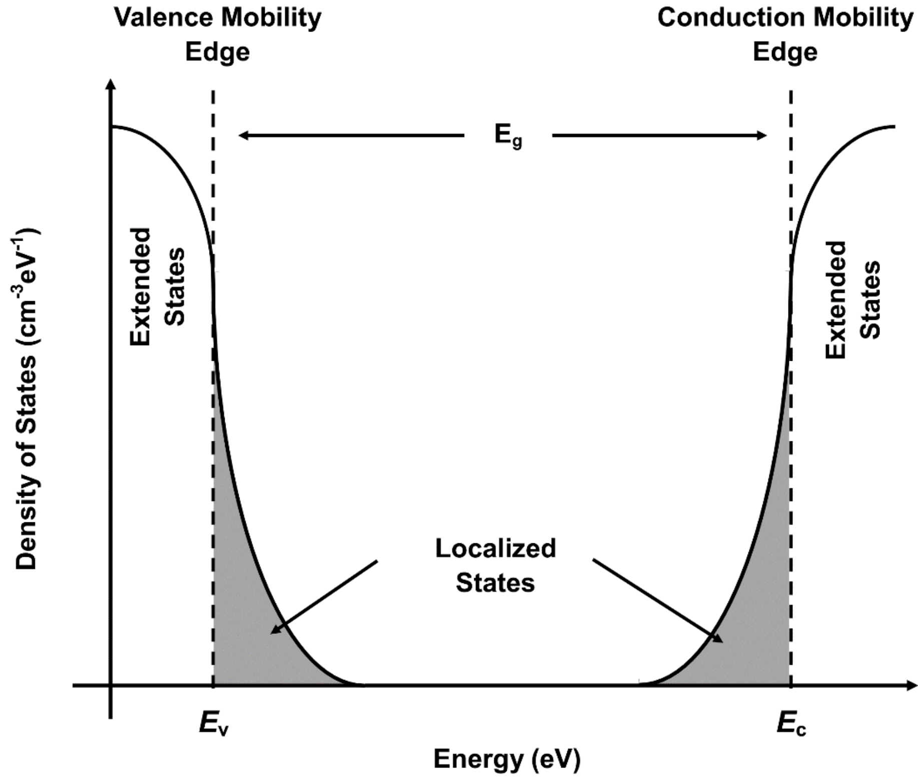

Figure 1.6. *The density of states (DOS) plotted as a function of energy for a typical disordered semiconductor. Here localised states form band tails.*

States within the band tails play a significant role in charge conduction [21]. At low temperatures, or at very high localised state concentrations, the transport of charge carriers is dominated by so-called 'hopping transitions' [21], where conduction occurs through tunneling from one localised state to another. However, at sufficiently low localised state concentrations and operational temperatures relevant for direct conversion detectors (near room temperature), transport is typically governed by multiple trapping (MT) [21], [22]. According to the MT model, inelastic scattering of moving carriers in the extended states occurs at nearly every atomic site and causes fast trapping into localized band-tail states below the mobility edge for electrons and above the mobility edge for holes. Trapping immobilizes carriers for a certain length of time (τ_{trap}).

Further propagation is determined by thermal reemission followed by new capture. The drift mobility μ_D relates to microscopic mobility μ_0 by

$$\mu_D = \mu_0/(1 + f_{trap}). \quad (1.1)$$

Where f_{trap} is the ratio of the time that the carrier spends in localized traps to that spent in mobile states, expressed as;

$$f_{trap} = \tau_{trap}/\tau_{free}. \quad (1.2)$$

If the time spent in the trap is much greater than the time the hole is free, then the drift mobility:

$$\mu_D = \mu_0 \tau_{free}/\tau_{trap}. \quad (1.3)$$

Since the release of trapped holes is thermally activated process, the ratio of free to trapped carriers changes with temperature, resulting in a temperature activated behavior of the mobility. MT transport of both electrons and holes is illustrated in Figure 1.7**.**

At strong electric fields, the release from traps can be assisted by field-induced tunnelling [22], meaning that it occurs with the energy deficit ΔE, as compared to the trap depth E, and is accompanied by tunneling over the distance $x = \Delta E/(eF)$ under the triangle energy barrier as schematically shown in the insert to Figure 1.7.

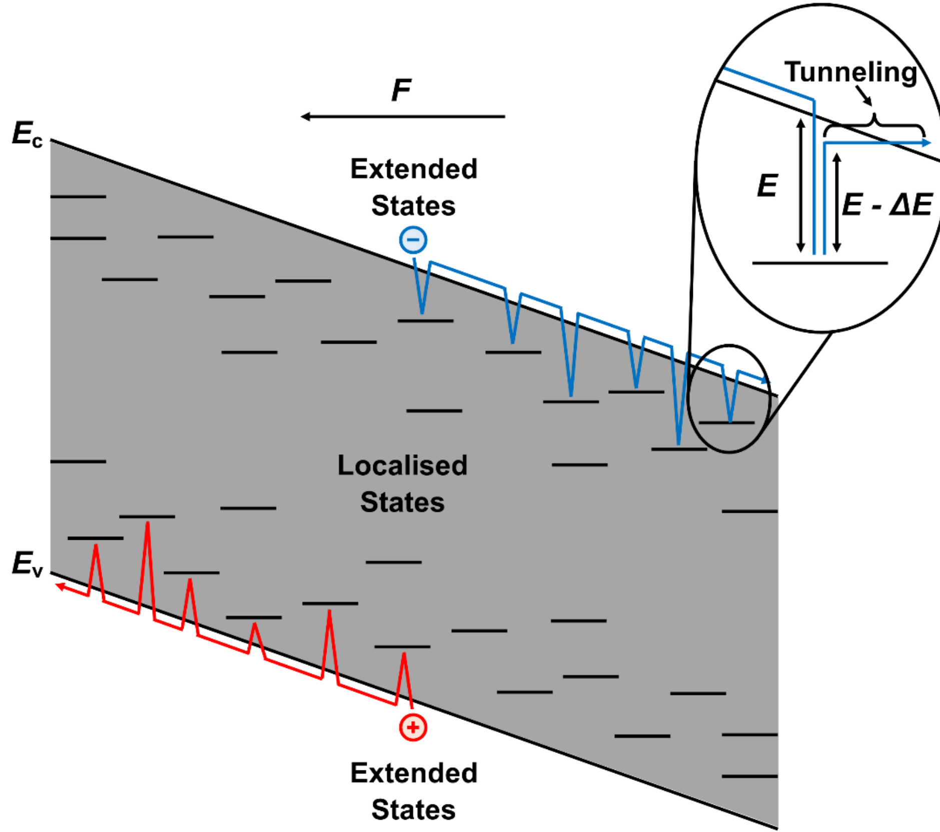

Figure 1.7*. An illustration of the multiple trapping (MT) transport process. The magnified portion displays field-assisted tunneling that lowers the activation energy to escape from a localised state.*

The effect of a high applied field on charge mobility in the MT transport regime was observed to play a similar role to temperature (T) [21], [22]. An effective temperature (T_{eff}) is introduced to account for the behaviour of μ with respect to F. An expression for T_{eff} is derived through numerical calculations and computer simulations [21] and is given as:

$$T_{eff} = \left[T^2 + (\gamma \frac{eF\alpha}{k})^2\right]^{\frac{1}{2}}. \tag{1.4}$$

In equation 1.4, γ is a dimensionless coefficient, a is localization length of trapping states in the band tail and k is Boltzmann's constant. Since the release from traps is activation assisted,

replacing T with T_{eff}, makes both the time that the carrier spends in localized traps and drift mobility to be dependent on T_{eff} ($\mu(T_{eff})$):

$$\mu(T_{eff}) \sim exp\left[\frac{-\varepsilon_a}{kT_{eff}}\right]. \tag{1.5}$$

Where ε_a is the average activation energy needed for charge to escape from shallow localised states within the mobility gap.

1.5 Dark Current (DC)

Due to the low mobility inherent to disordered photoconductors, a large applied field is necessary to achieve long enough schubweg to avoid depth-dependent collection efficiency of the X-ray-generated EHP. A typical operating applied field of 10 V/μm is necessary for photoconductors utilized in direct conversion X-ray detectors [6]. The consequence of this high applied field is that an appreciable leakage current flows through the detector structure, even in the absence of irradiation, deemed DC. DC is a source of system noise that constricts the dynamic range, inhibits quantum-noise-limited operation, and degrades the signal-to-noise ratio (SNR) of a detector. Negating DC's detrimental effects is of significant importance for high-resolution low-dose X-ray imagers, where the number of X-rays available to form each image is limited, and electronic system noise becomes a concern. A possible strategy to meet the requirements of high SNR falls into two categories: one is to decrease the electronic noise; the other is to increase the X-ray to charge conversion gain so that the X-ray quantum noise can overcome the electronic noise. In the first case, the electronic noise can be significantly decreased with the use of an image readout technique based on crystalline silicon (c-Si) CMOS AMA. c-Si CMOS technology is inherently less noisy and faster than a-Si:H technology. Another key benefit of c-Si technology is the high degree of integration possible [23]; the array peripheral circuitry (such as multiplexers,

charge amplifiers, double sampling, and analog-to-digital conversion circuits) can be integrated directly on the flat panel, thus improving SNR. In contrast, large-area, a-Si flat panel imagers must interface with peripheral circuitry (usually integrated into c-Si CMOS) to convert the a-Si pixel output into a format amenable to image processing. Unfortunately, these advantages of CMOS readout are accompanied by a significant increase in price, especially when it comes to large-area detectors.

Our approach is to focus on the latter case, i.e., to use an a-PbO-based X-ray-to-charge transducer to improve conversion gain in a-Si:H TFT based FPXI by 5 to 7 times in comparison with similar a-Se FPXI. However, accumulation of dark carriers in the TFT storage capacitors should not significantly add to the TFT pixel noise. The TFT array is commonly cited as contributing ~ 1500 electrons/pixel for arrays with a pixel size of ~ 100 x 100 μm^2, but this is manufacturing dependent and can vary from 1000 – 2000 electrons/pixel [24], [25]. Thus, DC should be tailored to suit the operational requirements of the detector system to reduce noise.

In terms of electronic noise accumulated in the TFT storage capacitors a rough estimate can be obtained. For example, a high-resolution fluoroscopic imaging system with a pixel size of 100 x 100 μm^2 and a readout time of 0.033 s (30 frames/second), a requirement that the accumulations of dark carriers in the storage capacitors should not exceed 2000 electrons suggests that DC should be less than 1 pA/mm^2. In terms of the lowest exposure necessary the tolerable levels of DC can be justified from the following considerations: In an ideal detector system, the noise produced by the photoconductor layer would be quantum-noise limited. This means that the quantum noise resulting from the stochastic nature of X-ray production and detection should be much greater than the noise contributed by DC. Using this condition, one can estimate the highest acceptable magnitude of DC. Selecting a minimum exposure (X_{min}) that the detector should operate

at, one can correlate this to an X-ray beam's fluence (φ). The quantum noise of this beam is $(\varphi A)^{1/2}$, where A is the area of a pixel. The number of X-rays absorbed within the photoconductor and subsequent EHP created is $((\alpha_{en}/\rho)/(\alpha/\rho))E_{ph}/W_{\pm}$, where α_{en}/ρ is the mass-energy linear attenuation coefficient, α/ρ is the mass linear attenuation coefficient, and E_{ph} is the energy of X-ray photon being absorbed. α_{en}/ρ, α/ρ, and $W_{\pm}$ are material-dependent parameters. This equation is simplified by approximating a real poly-energetic X-ray beam with a mono-energetic beam of X-rays. Assuming that DC contributes only shot noise (electronic noise caused by random fluctuations in current due to the discrete nature of charge carriers), the noise will be equal to $(J_{DC}At/e)^{1/2}$, where J_{DC} is DC density, e is the elementary charge, and t is the time during which the detector accumulates charge before reading out the signal. Therefore, as a first approximation, DC levels should meet the condition that:

$$J_{DC} \ll \left[\sqrt{\varphi A}\left(\frac{\alpha_{en}/\rho}{\alpha/\rho}\right)\frac{E_{ph}}{W_{\pm}}\right]^2 \frac{e}{At} \tag{1.6}$$

This approximation has been calculated before utilizing values for a-Se in [2]. In [2], the result obtained from equation 1.6, is J_{DC} << 60 pA/mm^2. Equation 1.3 assumes that DC contributes only shot noise, failing to account for 1/*f* (spectral density) noise, that is not negligible [2]. Estimating the magnitude of 1/*f* noise, DC should be as low as J_{DC} ~ 1 pA/mm^2 [2]. This agrees with the calculation of a maximum DC from the noise/pixel standpoint; the commonly cited range that J_{DC} must be maintained is below of 1–10 pA/mm^2 depending on application [2], [26]

1.5.1 Thermal Excitation

There are two components of DC: thermal excitation and subsequent drift of charge in the bulk of the photoconductor, and charge injection from biased electrodes. Bulk thermal generation of charge is an intrinsic property of the photoconductor. In narrow bandgap pure (undoped)

photoconductors, an electron from the VB can be thermally excited into the CB, leaving a hole in the VB. The probability of an interband excitation depends on the photoconductor's bandgap and the lattice's thermal energy.

In disordered photoconductors, various defects, such as dangling bonds and other lattice disorders, can introduce localized states of significantly high concentration within the mobility gap [21] as displayed in Figure 1.8. Since the probability of thermal excitation is proportional to the DOS and exponentially proportional to the activation energy, their certain combination can offer an alternate pathway for charge to be thermally excited from these localized states above the mobility edge.

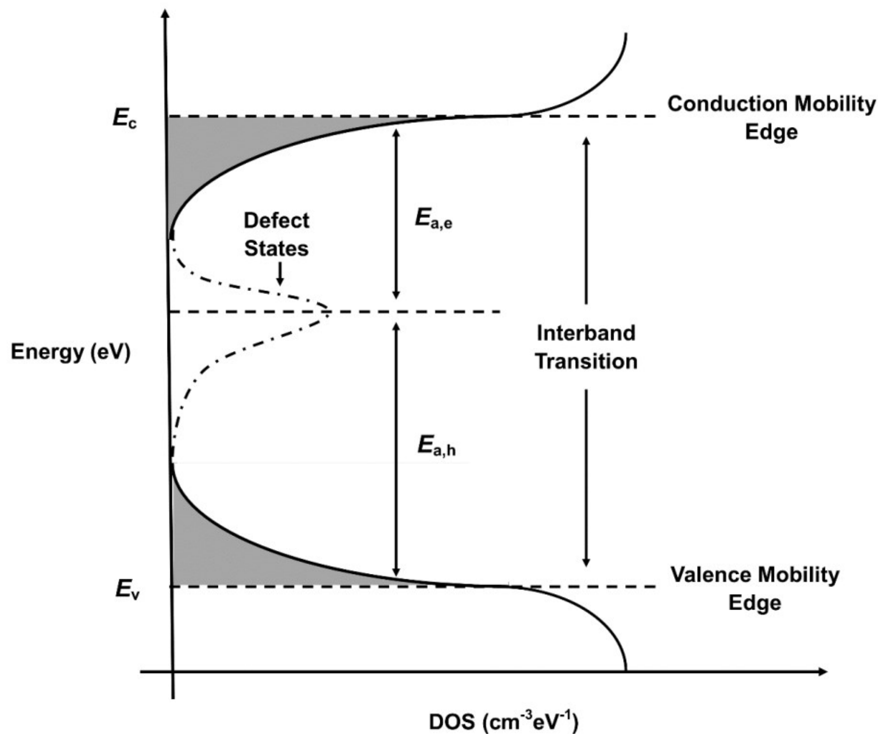

Figure 1.8. *The band-energy diagram of a disordered photoconductor with a peak in the DOS within the mobility gap, resulting from defect states. Here, thermal excitation can occur from an interband transition or from the defect states with a DOS.*

1.5.2 Injection

The other source of DC is the injection of charge carriers from biased electrodes. Injection depends heavily on the applied field across the detector structure and the electronic structure at the electrode/photoconductor interface. Under the influence of an applied field, either electrons or holes can be injected into the photoconductor. For charge to be injected into the photoconductor structure with a blocking (for example, reverse biased Schottky junction) contact, the charge carrier must overcome some potential barrier (refer to as a Schottky barrier) or tunnel through it, if it is sufficiently thin.

A Schottky barrier is formed upon the physical contact of a metal and a semiconductor. In Figure 1.9, a band diagram of the interface is depicted to show the formation of a Schottky barrier between a metal of work function $e\Phi_m$ and an intrinsic semiconductor of an electron affinity $e\chi$ (which is smaller than $e\Phi_m$). Note, that Figure 1.9 depicts an ideal case when a semiconductor does not contain any charges at the interface so that the band structure of the surface is the same as that of the bulk and there is no band bending.

When in contact, electrons from the conduction band of the semiconductor, which have higher energy than the metal electrons, will flow into the metal until thermal equilibrium is reached and the Fermi levels (E_F) on the two sides align [27]. As the electrons move out of the semiconductor into the metal, the free electron concentration in the semiconductor near the boundary decreases. This establishes a depletion region at the interface resulting in the band structure of the semiconductor bending. An energetic barrier is established at the interface of the two materials. The conventional Schottky barrier model assumes a uniform charge depletion region on the semiconductor side and a charge accumulation layer localised at the interface, resulting in a parabolic bending of the semiconductor bands. The exact curvature of the

band structure will depend on the position of the Fermi level of the semiconductor ($E_{F,S}$) with respect to the position of the Fermi level of the metal ($E_{F,M}$). In the case depicted in Figure 1.9, a Schottky barrier is formed that blocks the injection of electrons into the semiconductor. In the ideal case, the barrier height ($e\Phi_B$) is determined by the difference between the work function ($e\Phi_m$) of the metal and the electron affinity energy ($e\chi$) of the semiconductor [28], [29]. The quantum transmission of electrons or holes across the Schottky barrier is determined by two quantities: the barrier height and, more importantly, the decay length of the band bending. Together, these quantities determine the probability of transmission and the energy distribution of hot carriers across the metal-semiconductor interface.

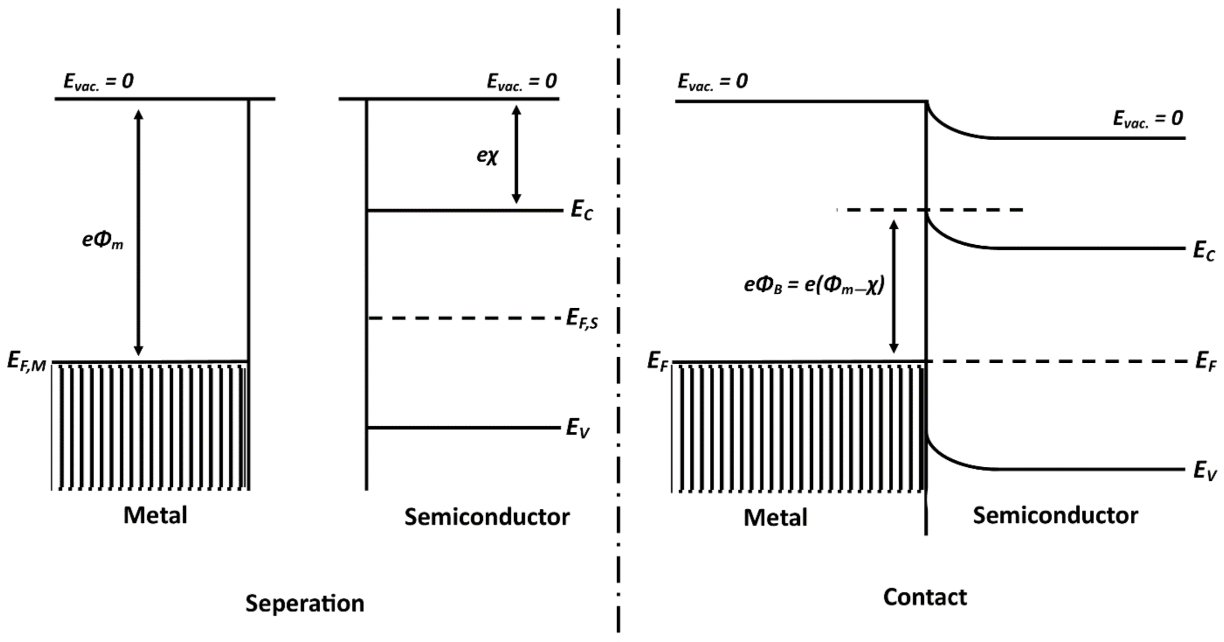

***Figure 1.9**. The formation of a Schottky barrier upon physical connection of a metal and a semiconductor. Here $E_{F,S} > E_{F,M}$, and as a result the band structure of the semiconductor bends up at the interface.*

Applying an external field will alter the shape of the potential barrier at the interface. As an example, if a negative bias is applied to the metal, it would decrease the barrier, increasing the probability of electron injection. The applied field alters the height of the barrier via the interactions between two forces: the force induced on the electron by the electric field and the image lowering force. To examine these forces, it is helpful to first look at an electron escaping a metal in a vacuum. The minimum energy an electron must have to escape the metal is $e\Phi_m$. Once the electron escapes the metal surface, it induces a positive charge on the surface of the metal. The attractive force between the electron and the induced charge is equivalent to the force between a positive charge at a distance +x and a negative charge at a distance -x from the surface of the metal. Therefore, the image force on the electron is:

$$Force_{image} = \frac{-e^2}{16\pi\varepsilon_0 x^2}, \tag{1.7}$$

where e is the elementary charge and ε_0 is the permittivity of a vacuum [27]. The work done on the electron to move it from infinity far away to the position x relative to the metal is:

$$E_{image}(x) = \frac{-e^2}{16\pi\varepsilon_0 x} \tag{1.8}$$

[27]. Now if a field is applied, the potential energy of the electron is the summation of the potential of the field image force potential, expressed as:

$$PE(x) = \frac{-e^2}{16\pi\varepsilon_0 x} - e|F|x \tag{1.9}$$

[27]. The potential of an electron as a function of the distance x, from the metal surface is illustrated in Figure 1.10**.**

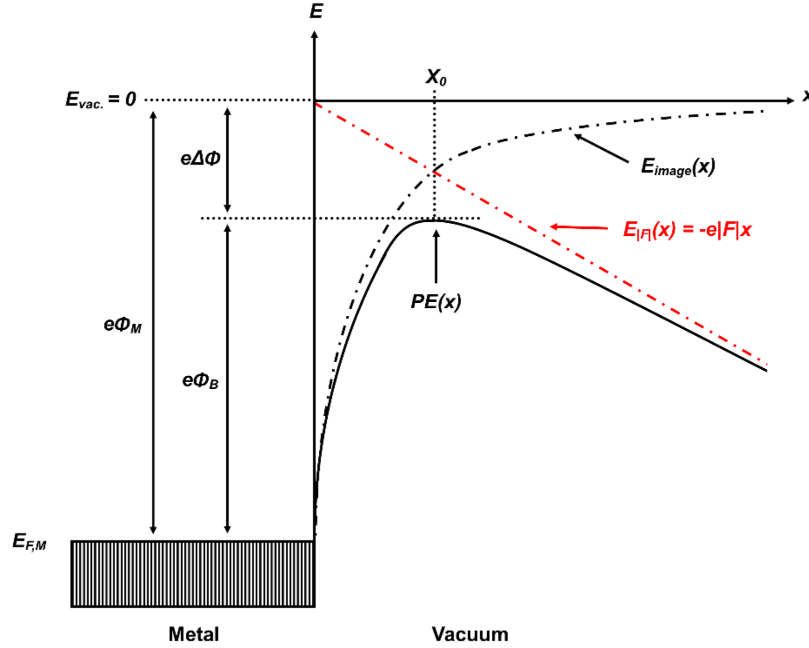

***Figure 1.10**. The potential on an electron near the surface of a negatively biased metal in a vacuum. The application of a negative bias lowers the barrier height an electron must overcome to escape the metal by a factor of eΔΦ. The barrier is lowered by the interaction of the image lowering energy and the potential energy of the field.*

The position x_0 can be found by taking the first derivative of *PE(x)* with respect to *x*, setting it equal to 0, and solving for *x*. x_0 is equal to:

$$x_0 = \sqrt{\frac{e}{16\pi\varepsilon_0|F|}} \tag{1.10}$$

[27]. Inserting x_0 in *PE(x)*, the factor *eΔΦ* is found and given by:

$$e\Delta\phi = \sqrt{\frac{e^3|F|}{4\pi\varepsilon_0}} = \beta_S\sqrt{|F|}, \tag{1.11}$$

where β_S is the so-called Schottky coefficient [27]. Here, a change in the applied field shifts x_0, changing $e\Delta\Phi$ and the effective barrier height. In this way it is clear to see that the height of a Schottky barrier is directly proportional to the applied field.

The equations derived for an electron escaping the surface of a metal into a vacuum are applicable to a metal interfaced with a semiconductor. ε_0 in equations 1.4 – 1.8 must be replaced with $\varepsilon_r\varepsilon_0$, where ε_r is the relative permittivity coefficient of the semiconductor. In a metal-semiconductor system, a depletion region is established that induces some built-in potential at thermal equilibrium that slightly lowers the effective barrier height ($e\Phi_{B,0}$) to $e\Phi_{B,Therm}$. Figure 1.11 illustrates the effect an applied field has on a Schottky barrier at the interface of a metal and a semiconductor.

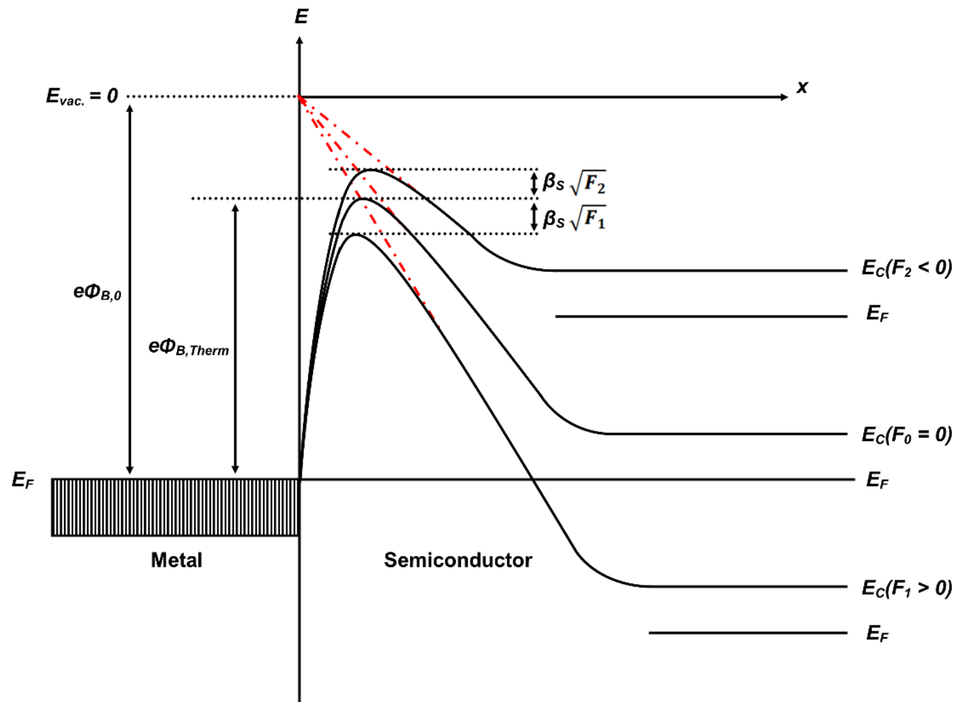

Figure 1.11*. Energy-band diagram for a metal interfaced with an n-type semiconductor under different applied fields. F > 0 refers to a field that points from semiconductor to the metal (right to left).* $F_1 > 0$ *lowers* $e\Phi_{B,Therm}$ *by* $\beta_S\sqrt{F_1}$ *and* $F_2 < 0$ *increases* $e\Phi_{B,Therm}$ *by* $\beta_S\sqrt{F_2}$.

Examination of Schottky interfaces allows a deeper understanding of the injection component of DC. In Figure 1.4, one can see that within a detector structure, there are two locations at which a Schottky barrier can arise: at the photoconductor/top electrode and the photoconductor/charge collecting electrodes interfaces. These interfaces can be a source of injection, depending on the electronic properties of the photoconductor and the electrode. The value of the work function of the metal utilized for the electrodes will affect Φ_B and, therefore, injection.

Although crystalline semiconductors with a well-defined band diagram were considered above, the Schottky barrier model is also applicable to the interfaces between disordered (amorphous) semiconductors and metal contacts. When the metal and the surface of an amorphous semiconductor are in close contact, the delocalized electronic states around the Fermi level responsible for electrical conduction in the metal, are coupled to the delocalized electronic states for electrons or holes near their respective mobility edges in the amorphous semiconductor. Because in amorphous semiconductors the Fermi level is pinned around the middle of the mobility gap, the lowest-lying delocalized states in a semiconductor that can communicate with electrons in the metal are now at an energy offset above the Fermi level. Like in the case of crystalline semiconductors, this energy offset manifests itself as a potential energy barrier for charge transport across the metal-semiconductor interface

1.6 Blocking Layers to Suppress DC

Since DC consists of thermal generation (an intrinsic property of the photoconductor) and injection (an operational property of the detector structure), an engineering solution to suppress DC must be targeted to decrease injection. In a-Se detectors, injection was decreased by placing a thin blocking layer between the electrodes and the photoconductor. The blocking layer had to

decrease the injection of one type of charge carrier from the electrode while simultaneously allowing the passage of photogenerated charge carriers of the opposite polarity. For example, a blocking layer placed between a positively biased electrode and a photoconductor must be able to block the injections of holes while letting photogenerated electrons transport through the layer and be collected by the electrode. Therefore, blocking layers can be categorized into hole blocking and electron blocking layers, as seen in Figure 1.12. Electron and hole blocking layers can be employed in the same detector structure to block the injection of both species of charge carriers. This is unnecessary in certain detector structures since the μ of electrons and holes are often different, and it is only necessary to block the injection of the more mobile charge carrier.

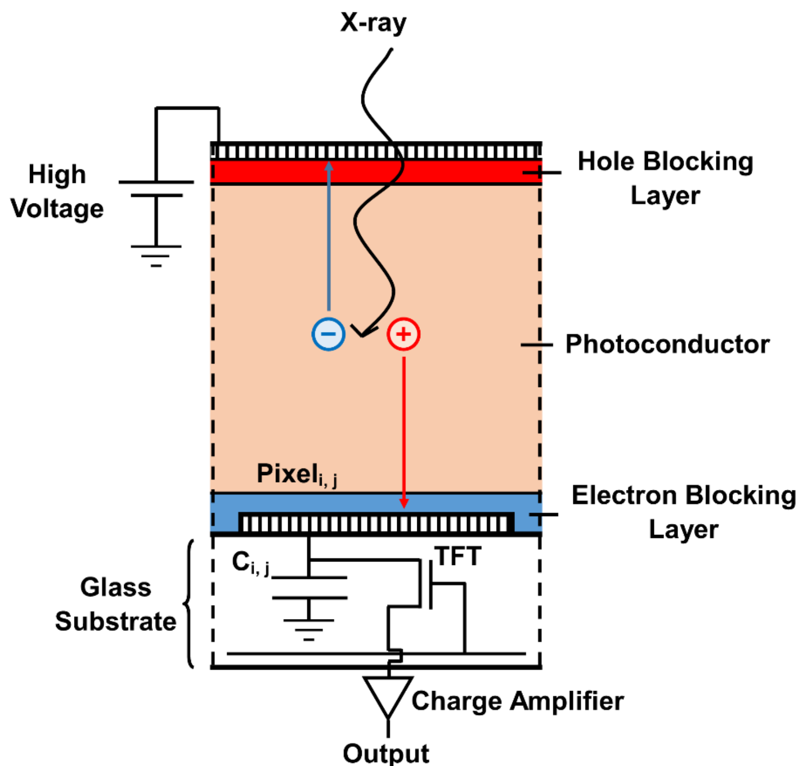

Figure 1.12. *An illustration of a detector with both an electron and hole blocking layers present in its structure. The blocking layers here prevent the injection of one species of charge while allowing photogenerated charge of the opposite polarity to pass.*

1.6.1 Doped/Alloyed a-Se (p-like and n-like)

The DC problem in the direct conversion a-Se FPXIs was solved by the introduction of carefully designed blocking layers at the electrodes, thus creating a-Se multilayered structures. The DC in these multilayered a-Se detectors was brought down by three orders of magnitude in comparison with that in a single a-Se layer [2] making the development of a-Se multilayered blocking structure one of the most important milestone achievements in the development of FPXIs. Conventionally, these a-Se multilayered detectors consist of an intrinsic 200 – 1000 μm thick [30] photoconductive layer of stabilized a-Se (a-Se:0.2% – 0.5% As + 10 – 40 ppm Cl [31], [32]) labeled as the *i*-layer, sandwiched between two thin blocking layers of doped or alloyed a-Se [33]. The blocking layers were either *n*-like or *p*-like depending on the charge carrier transport properties that they possess, rather than the position of the Fermi-level, as in classical semiconducting physics [31], [33]. *n*-like blocking layers usually consist of a-Se doped with an alkali metal such as Na [34]. The transport properties of *n*-like blocking layers are characterized by a hole schubweg << electron schubweg ($\mu_h\tau_h F \ll \mu_e\tau_e F$), where subscripts *e* and *h* refer to electrons and holes, respectively [35]. Effectively, injected holes are immediately trapped, and photogenerated electrons drift freely through the *n*-like layer. *p-like* blocking layers commonly consist of a thin layer of a-Se alloyed with As (As_2Se_3) that have carrier schubwegs such that ($\mu_h\tau_h F \gg \mu_e\tau_e F$), effectively blocking injected electrons and allowing the passage of photogenerated holes [31]. Multilayered a-Se detectors are labeled *n-i-p*, *n-i,* or *p-i*, referring to the blocking layer(s) present in its structure.

This multilayered approach where the photoconductor is doped to alter its properties can be extended to direct conversion detectors based on other photoconductors. *n*-like and *p*-like blocking layers have beneficial characteristics that make them practical to a-Se detectors. Both *n*-

like and *p*-like blocking layers consist of dope or alloyed photoconductor material; therefore, the electric permittivity of the entire structure is equivalent. This means that the applied voltage will drop linearly, and the resulting electric field will be constant across the structure. It is important to note that a uniform electric field within the structure is only accurate at the instant of bias application. As charge is injected from the bias electrodes, it becomes trapped with the adjacent blocking layers. Specifically, holes injected from the positive contact become trapped in the *n*-like layer, and electrons injected from the negative contact become trapped in the *p*-like layer. The space charge is built-up within the *n*-like and *p*-like layers and modifies (screens) the electric field at the electrode/blocking layer interface(s) [33]. The actual fields at the positive and negative metal contacts become lower than the corresponding values in the intrinsic layer, and hence the rates of hole and electron injection are significantly diminished. Another benefit is that the blocking layer(s) and the *i*-layer are of the same material, which has the advantage of greater compatibility with the charge transport layer. This will limit charge trapping effects at the interfaces, which is crucial for real-time operation.

However, *p*-like*,* and *n*-like layers have significant drawbacks that deter their implementation to direct conversion detectors based on other photoconductors. *p*-like*,* and *n*-like layers are technically complex to develop; even if the concept of *p*-like and *n*-like layers applies to a photoconductor and technologically feasible, its implementation requires a co-thermal vacuum deposition process, where multiple crucibles containing the appropriate mixture of materials to produce each layer are in the same vacuum chamber [34]. This process yields charge carrier transport properties that heavily depend on the type and concentration of dopant material, as well as any contaminants and impurities. *p*-like and *n*-like blocking layers have to be a minimum thickness (L) of $\geq 10 - 15$ μm [34] so that the schubweg of the blocked charge carrier is less than

the layer thickness ($L > \mu\tau F$). In addition, *p-like* and *n-like* blocking layers are less effective in suppressing DC when detectors are biased at fields > 10 V/μm [36].

1.6.2 Oxides (TiO_2 and CeO_2)

Thin films of wide bandgap oxides are used in many applications, including serving as blocking layers (to block the injection of charge from biased electrodes). CeO_2 and TiO_2 have been used as hole blocking layers in a-Se-based detectors and perovskite solar cells [36]–[40]. CeO_2 and TiO_2 are both *n*-type semiconductors that have wide bandgaps of 3.3 eV [37], [39] and 3.2 eV [36], [40], respectively. When interfaced with an indium tin oxide (ITO) electrode, CeO_2 forms a potential barrier of 2.8 eV seen by holes injected from the metal [37]. When TiO_2 is interfaced with fluorine-doped tin oxide (FTO), it forms a potential barrier of 2.8 eV [40]. In both cases, the oxide forms a potential barrier that is large enough to suppress the injection of holes to negligible levels. Depending on the photoconductor interfaced with the oxide, photogenerated electrons experience little to no potential barrier so that they can pass without hindrance.

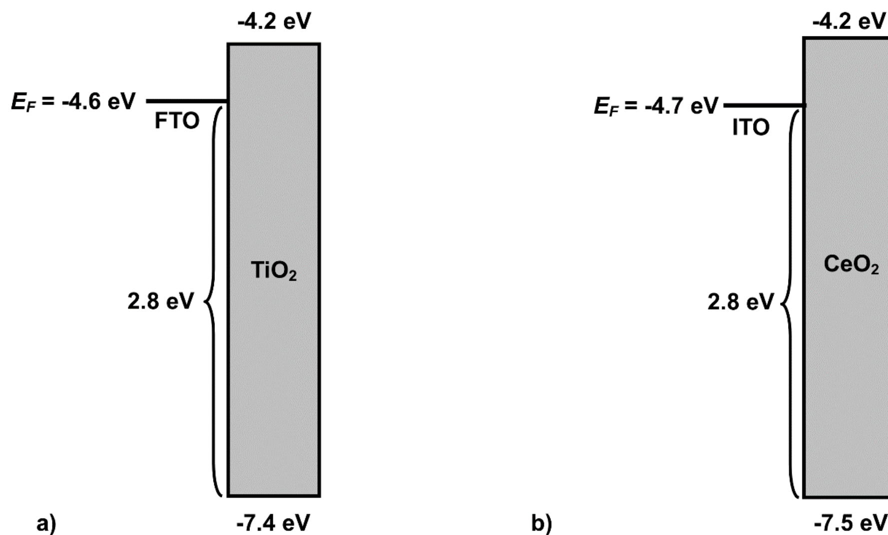

***Figure 1.13**. An energy level schematic of a) FTO interfaced with TiO_2 and b) ITO interfaced with CeO_2.*

Unlike *p*-like and *n*-like blocking layers, where injected charge is trapped with the layer, oxides prevent injection altogether by creating a large potential barrier at the electrode/blocking layer interface. Oxides do not rely on trapping injected carriers, meaning there is no requirement to be a certain thickness, given the thickness is enough to inhibit quantum tunneling. Oxide layers can be as thin as 10–30 nm [36]–[38]. The dielectric permittivity of these oxide layers can differ slightly from an intrinsic photoconductive layer. However, because they are quite thin, it can be assumed that the applied electric field is uniform throughout the layers [41]. TiO_2 and CeO_2 layers are deposited by oxygen-ion-assisted electron-beam (e-beam) deposition [36]. Although very efficient in blocking hole injection for small area detectors such as high-gain avalanche rushing photoconductor (HARP) a-Se detectors, neither TiO_2 nor CeO_2 is technologically feasible to be used in large area FPXI.

1.6.3 Sb_2S_3

Hole blocking oxide layers are often paired with an Sb_2S_3 electron blocking layer in the same detector structure [36]–[38], [41]. Sb_2S_3 relies on the same mechanisms as *p*-like layers in that Sb_2S_3 contains many states that trap electrons [38]. After an external field is applied to the detector structure, electrons accumulate within the Sb_2S_3 layer forming a region of negative space charge that repels electrons from being injected from the adjacent electrode [38]. CeO_2 – a-Se – Sb_2S_3 is often used in HARP a-Se detectors [38]. In HARP detectors, a substantial bias ($F \geq 70$ V/µm) [42] is applied to the detector to achieve avalanche multiplication of charge, thus necessitating sufficient DC suppression.

Blocking layers of Sb_2S_3 must be thicker than oxide layers because they rely on trapping injected charge carriers. A thickness of 0.5 µm of Sb_2S_3 is sufficient to block the injection of electrons in an a-Se HARP detector structure [38].

1.6.4 Polymers (PI and PTCBI)

Certain polymers including polyimide (PI) [26], [36], [43], and perylene tetracarboxylic bisbenzimidazole (PTCBI) [36], [41] have demonstrated their effectiveness as hole blocking layers and lack the above-mentioned problems inherent to *p-like* and *n-like* layers [36], [37]. PTCBI and PI are shown to have hole blocking properties, analogous to *n*-like blocking layers [36], [44]. PI and PTCBI are large bandgap semi-insulators that have very low hole mobilities [36], [44]. PI is a polymer commonly used in electronics as an insulator due to its large bandgap and excellent mechanical properties, such as high heat resistance and low moisture uptake [45], [46]. In addition to PI's ideally suited electrical properties as an *n-like* blocking layer alternative, its application process of simple spin-coating (depicted in Figure 1.14) is much more achievable and simpler compared to the application process of conventional *p-like* or *n-like* blocking layers. PTCBI is not as simple to deposit compared to PI. PTCBI requires a process similar to thermal PVD but is performed at a lower vacuum of 0.1 torr, compared to ~ 10^{-5} torr for thermal PVD [47].

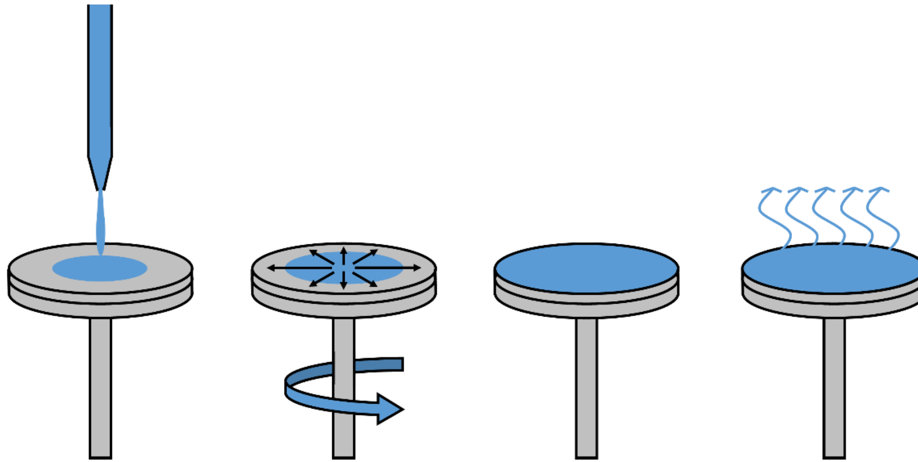

***Figure 1.14**. The spin coating process used to deposit PI. A controlled amount of PI is dropped onto a substrate, the substrate is the spun at a high rpm that causes the PI to evenly spread out into a uniform layer, and then the substate is heated to evaporate the solvents, curing the PI.*

Preliminary results suggest [38], [48] that PI and PTCBI layers have the potential as a practical solution to the DC problem in a variety of X-ray photoconductors however, their properties and deposition processes have to be optimized. Similar to *n*-like blocking layers, PI and PTCBI must be a certain thickness so that holes are trapped before they can transit the material. This is coupled with the fact that PI and PTCBI are highly resistive materials and thus a large portion of the applied bias to the detector structure will drop over them.

1.7 PI/a-PbO Detectors

Enhancing the blocking characteristics of a-PbO detectors requires the development of hole blocking layers. In fact, holes are shown to be the much faster charge carrier in poly-PbO [49], [50]. Therefore, the injection of holes from positively biased electrodes is believed to be the primary component of DC in a-PbO detectors. The feasible and well-controlled deposition process and compatibility with FPXI technology makes PI a practical approach for the development of an a-PbO-based X-ray-to-charge transducer with extremely low DC for applications in direct conversion X-ray imaging detectors. There is a possibility of incompatibility of polymers with the requirements of real-time imaging since they may enhance charge trapping at the polymer/a-PbO interface causing signal lag and deteriorating temporal performance. However, previous experience with a thin (1-5 μm) layer of PI or cellulose acetate as a blocking layer for a-Se [36], [48] was very encouraging: no deterioration of temporal performance was found while DC was reduced by an order of magnitude.

For the design of our PI/a-PbO detector, a thin layer (1.1 μm) of PI is spin coated onto an ITO substrate before a thick layer (18.5 μm) of a-PbO is deposited with ion assisted thermal PVD. A thickness of 1.1 μm of PI was chosen as a starting point because it was found to be adequate to suppress DC while not being too thick as to have a substantial fraction of applied voltage drop

over it, in a PI/a-Se detector [43] and therefore should behave similarity in a PI/a-PbO structure. The PI blocking layer not only suppresses DC in the PI/a-PbO, but it also solves another problem with a-PbO deposition. PI improves the adhesion of a-PbO to the substrate, which has been observed to be a problem when depositing layers of a-PbO thicker than ~ 10 μm onto ITO-coated glass substrates. A PI/a-PbO detector is shown in Figure 1.15.

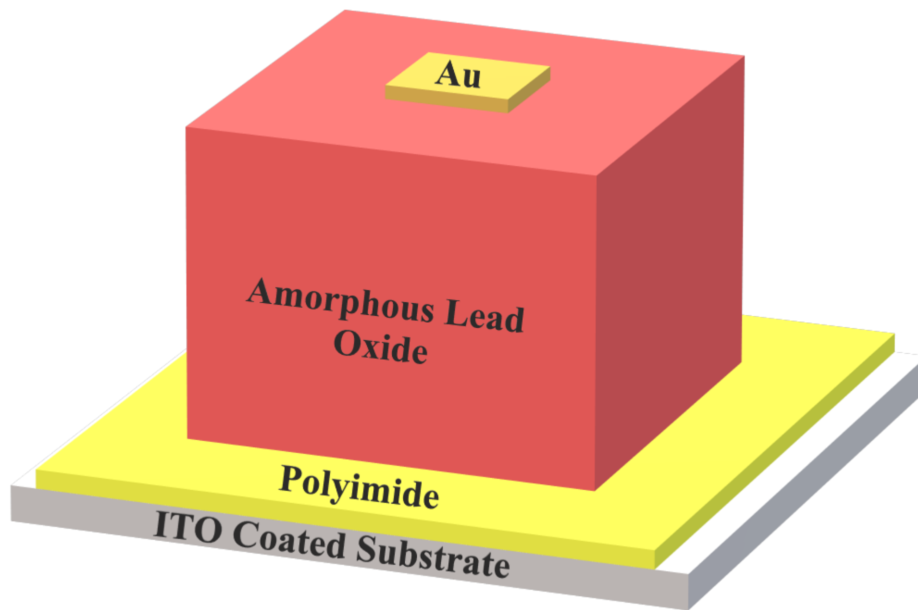

Figure 1.15. *A prototype direct conversion detector that utilizes a-PbO as an X-ray–to–charge transducer and a PI hole blocking layer (not to scale).*

Indeed, a PI blocking layer both suppresses DC and improves adhesion between a-PbO and the substrates, however, for future iterations of PbO-based detectors the structure needs to be individually optimized. The thickness of the PI layer should be tailored for each PI/a-PbO detector to ensure a balance between DC suppression to tolerable levels and the fraction of applied voltage that drops over it rather than the a-PbO layer. It must also be investigated if PI degrades the detector's performance by creating an interface between itself and the

photoconductor. An investigation was launched that reported on the temporal performance, X-ray sensitivity, and transient DC behavior of the PI/a-PbO detector. A mathematical model was developed to simulate the experimentally measured transient DC decay and used to investigate the mechanisms of DC.

Chapter 2: Dark Current Modeling for a Polyimide – Amorphous Lead Oxide-based Direct Conversion X-ray Detector

This topic has been elaborated in the following publication:

T. Thibault, O. Grynko, E. Pineau, and A. Reznik, "Dark Current Modeling for a Polyimide - Amorphous Lead Oxide-based Direct Conversion X-ray Dtector," *Sensors*, 2022.

The full text of the publication is listed below.

Dark Current Modeling for a Polyimide - Amorphous Lead Oxide-based Direct Conversion X-ray Detector

Tristen Thibault[1,*], Oleksandr Grynko[1], Emma Pineau[1], and Alla Reznik[1,2]

[1] Department of Physics, Lakehead University, Thunder Bay, ON P7B 5E1, Canada; ogrynko@lakeheadu.ca (O.G), enpineau@lakeheadu.ca (E.P), areznik@lakeheadu.ca (A.R)

[2] Thunder Bay Regional Health Research Institute, Thunder Bay, ON P7B 6V4, Canada

* Correspondence: ttthibau@lakeheadu.ca

Abstract: The reduction of the dark current (DC) to a tolerable level in amorphous selenium (a-Se) X-ray photoconductors was one of the key factors that led to the successful commercialization of a-Se-based direct conversion flat panel X-ray imagers (FPXIs) and their widespread clinical use. Here, we discuss the origin of DC in another X-ray photoconductive structure that utilizes amorphous lead oxide (a-PbO) as an X-ray-to-charge transducer and polyimide (PI) as a blocking

layer. The transient DC in a PI/a-PbO detector is measured at different applied electric fields (5–20 V/μm). The experimental results are used to develop a theoretical model describing the electric field-dependent transient behavior of DC. The results of the DC kinetics modeling show that the DC, shortly after the bias application, is primarily controlled by the injection of holes from the positively biased electrode and gradually decays with time to a steady-state value. DC decays by the overarching mechanism of an electric field redistribution, caused by the accumulation of trapped holes in deep localized states within the bulk of PI. Thermal generation and subsequent multiple-trapping (MT) controlled transport of holes within the a-PbO layer governs the steady-state value at all the applied fields investigated here, except for the largest applied field of 20 V/μm. This suggests that a thicker layer of PI would be more optimal to suppress DC in the PI/a-PbO detector presented here. The model can be used to find an approximate optimal thickness of PI for future iterations of PI/a-PbO detectors without the need for time and labor-intensive experimental trial and error. In addition, we show that accounting for the field-induced charge carrier release from traps, enhanced by charge hopping transitions between the traps, yields an excellent fit between the experimental and simulated results, thus, clarifying the dynamic process of reaching a steady-state occupancy level of the deep localized states in the PI. Practically, the electric field redistribution causes the internal field to increase in magnitude in the a-PbO layer, thus improving charge collection efficiency and temporal performance over time, as confirmed by experimental results. The electric field redistribution can be implemented as a warm-up time for a-PbO-based detectors.

Keywords: Amorphous lead oxide; blocking layer; mathematical model; dark current; direct conversion; kinetics; polyimide; X-ray detector.

2.1 Introduction

Advanced direct conversion X-ray detectors utilize a layer of photoconductive material that acts as an X-ray-to-charge transducer, deposited over a large area imaging array [2], [3]. Metal electrodes are used to establish an electric field within the photoconductor [4]. In the only commercially implemented direct conversion detectors, which are based on amorphous selenium (a-Se) photoconductors [2], [31], a typical operating applied electric field is ≥10 V/µm. Such a strong electric field is needed to suppress mutual recombination of X-ray generated electron-hole pairs (ehp) and provide adequate charge collection efficiently. The dark current (DC) in such a metal/a-Se/metal photoconductive structure would be unacceptably large if preventative measures were not taken.

To suppress DC to acceptable levels (1–10 pA/mm^2 depending on application [2], [26]) in a-Se detectors, charge blocking layers are implemented [31], [33], [51]. Conventionally, a-Se photoconductive structures are multilayered, consisting of an intrinsic photoconductive layer of a-Se (*i*-layer) sandwiched between two charge blocking layers of doped or alloyed a-Se [33]: a thin (a few µm) alkali metal-doped a-Se layer blocks the injection of holes and allows the passage of photogenerated electrons, denoted as the *n*-like layer [35]; and a few µm thick As_2Se_3 *p*-like blocking layer blocks the injection of electrons and allows the passage of photogenerated holes [31].

Although practically used in a-Se detectors, *p*-like and *n*-like layers are technically complex to produce, requiring a co-thermal vacuum deposition process [34]. In addition, *p*-like and *n*-like blocking layers are less effective in suppressing DC when detectors are biased at fields >10 V/µm, which is needed to improve charge collection efficiency [36]. Recent research has shown that certain polymers (polyimide (PI) [38], cellulose acetate (CA) [36], and perylene

tetracarboxylic bisbenzimidazole (PTCBI) [44]) are promising candidates as blocking layers. These materials maintain effectiveness when detectors are biased at high fields, are technologically less complex to produce, and are compatible with large area flat panel detector technologies. That is, they can be coated uniformly on a large area imaging array so that the photoconductive layer is subsequently deposited directly onto blocking layers [36], [37], [44]. Among these potential candidates, PI stands out as it demonstrated its effectiveness when incorporated into practical a-Se detector structures: PI can maintain a sufficiently low DC (less than 10 pA/mm^2) even under a high electric field where impact ionization occurs in a-Se [48]. It was also shown that a PI blocking layer aids in the suppression of signal lag in a-Se detectors [36], [44]. Despite these encouraging results, the exact transport properties of PI interfaced with photoconductors in a detector structure are not well understood [43], and concerns remain that interfacing a foreign material such as PI with a photoconductor other than a-Se, could affect detector performance. Although it is very tempting to use the PI blocking layer in conjunction with an amorphous lead oxide (a-PbO) photoconductor [12], [13], [26], [52], it is challenging to predict the level of DC that will flow through a PI/a-PbO detector at a given time and electric field. Moreover, other factors affecting DC, such as possible charge accumulation at the PI/a-PbO interface, are needed to be understood. Furthermore, the PI/a-PbO detector must maintain the fast X-ray response inherent to a-PbO detectors [7] to ensure its feasibility for real-time imaging applications. Therefore, it is imperative to verify the low-lag (low residual signal after the termination of X-ray exposure) operation of the multilayered PI/a-PbO detector.

In this work, an a-PbO-based single-pixel detector prototype with a thin layer of PI (a “thin” layer refers to the fact that the blocking layer thickness is much smaller than the photoconductor thickness) positioned between the bottom electrode and the a-PbO layer is investigated in terms of

the temporal performance, sensitivity, and bias-dependent transient behavior of DC. DC kinetics in a PI/a-PbO detector is simulated via a mathematical model and fitted to experimental data to understand the kinetics and processes that govern the suppression of DC in PI/a-PbO photoconductive structures.

2.2 Materials and Methods

2.2.1 Detector Fabrication

A single-pixel PI/a-PbO X-ray detector [12], [26] has been fabricated as the prototype for an a-PbO-based direct conversion flat panel imager. In Figure 2.1a, a schematic diagram of the detector prototype structure is illustrated, and Figure 2.1b, an SEM cross-sectional image is shown. It was made in very few numbers of processing steps that included the use of a PI blocking layer. An indium-tin-oxide (ITO) coated glass slide was used as a substrate and a bottom electrode; it was cleaned thoroughly with acetone, methanol, and isopropanol and dried under N_2. A 1.1 µm thick PI layer was deposited on it by spin coating. A mask was utilized during the spin coating of PI to ensure a small area of ITO remains uncoated for the later purpose of electrical connection, essential for DC kinetics experiments. An 18.5 µm layer of a-PbO was then deposited using ion-assisted thermal deposition [19], [26] onto the PI-coated substrate. A gold contact of area ≈ 1 mm^2 and thickness of 20 nm was sputtered on top of the a-PbO, forming the top electrode. The smallest electrode determines the effective area of the detector, i.e., the Au contact; thus, the detector's pixel size is ≈1 mm^2. Previous publications [19], [26] contain a detailed description of the ITO substrate preparation, PI layer spin-coating, and a-PbO layer ion-assisted thermal deposition processes.

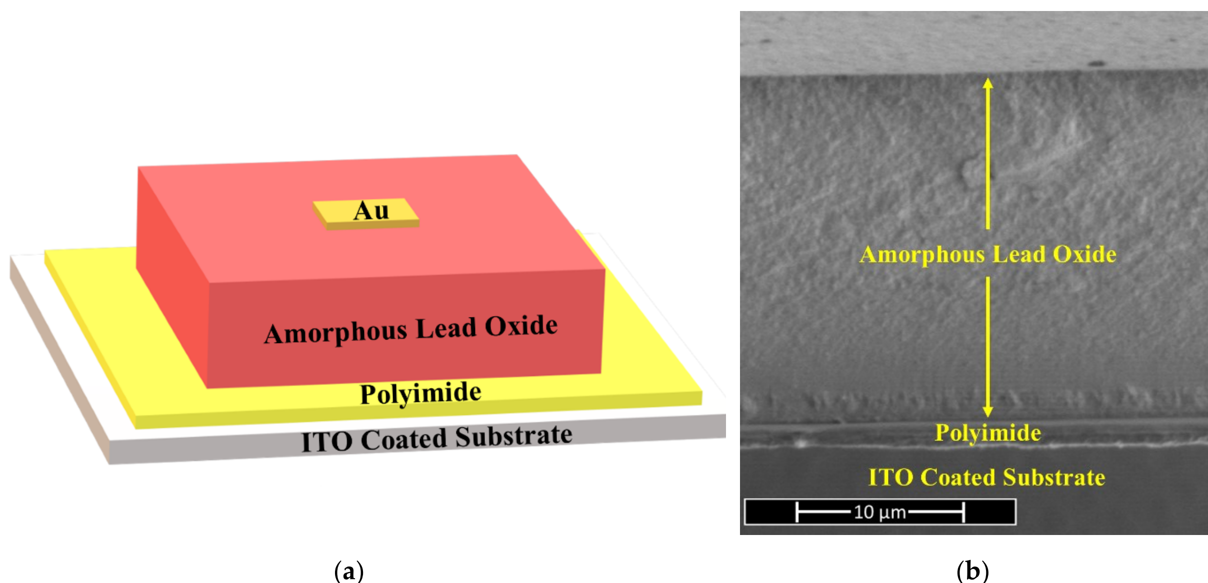

Figure 2.1 *a) Schematic diagram (not to scale) and b) a cross-sectional scanning electron microscopy (SEM) image of a single-pixel PI/a-PbO direct conversion X-ray detector.*

2.2.2 Experimental Setup – Temporal Performance and Sensitivity Characterization

Evaluation of temporal performance was conducted using an X-ray-induced photocurrent method (XPM) in continuous and modulated modes. In both modes, a biased single-pixel PI/a-PbO X-ray detector was exposed to either continuous or modulated X-ray pulses, and an X-ray-induced photocurrent was evaluated. The modulated mode of XPM was used to calculate signal lag [26]. Figure 2.2a shows a schematic of an experimental setup for a modulated XPM, where a PI/a-PbO detector is exposed to a sequence of short ≈ 16.67 ms X-ray pulses with a ≈ 16.67 ms interval between them. The pulsed irradiation was achieved by modulating a continuous X-ray pulse generated with a radiographic X-ray unit with a 0.3 mm thick copper chopper. The frequency of the chopper's modulation was 30 Hz, corresponding to the frame rate of 30 frames per second (fps) commonly used in fluoroscopy [53].

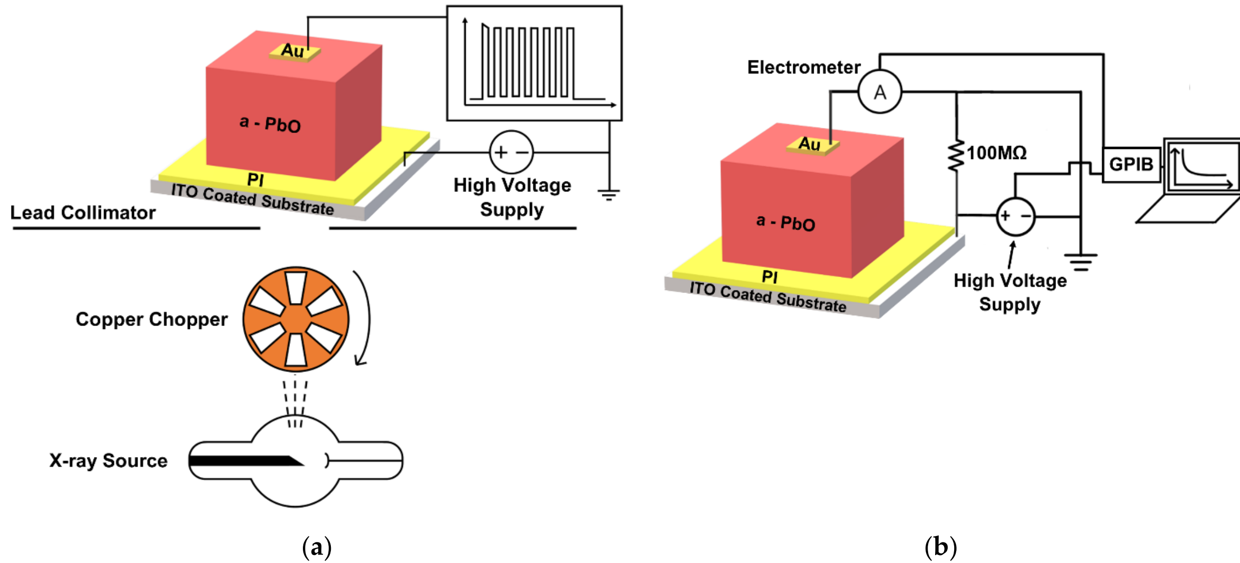

Figure 2.2. Experimental setups for a) modulated and continuous XPM and b) DC kinetics.

The continuous mode of XPM was used to evaluate detector sensitivity. Sensitivity to X-rays is characterized in terms of energy required to create a single detectable ehp ($W_{\pm}$). $W_{\pm}$ is derived from the total charge collected upon continuous X-ray exposure: the lower $W_{\pm}$ is, the higher is sensitivity. More details on this analysis can be found elsewhere [12], [18], [54]. In a-PbO, $W_{\pm}$ was found to depend on the applied electric field. As discussed later, it is believed that the electric field undergoes a redistribution within the PI/a-PbO detector after the application of a bias. Therefore, $W_{\pm}$ was measured by a series of successive pulses immediately after the application of a bias and compared to $W_{\pm}$ measured 10 min after bias application. In both cases (immediate irradiation and irradiation after 10 min), the sample was allowed to rest in a short-circuited fashion, releasing any previously trapped charge. The experimental configuration, seen in Figure 2.2a, was used for $W_{\pm}$ measurements with the condition that the chopper was fixed in the open state, allowing a continuous beam of irradiation to pass.

The PI/a-PbO detector was housed within an Al box and biased in positive polarity (positive voltage applied to the ITO contact) to a field of 20 V/μm with a Stanford Research

Systems PS350 power supply. To achieve the desired field (F_0), a bias of ($V_0 = F_0 \times (L_{PbO} + L_{PI})$) was applied to the sample, where L_{PbO} is the thickness of the a-PbO layer and L_{PI} is the thickness of the PI layer. The photocurrent was read out from the top Au contact with a Tektronix TDS 2024C oscilloscope with a 1 MΩ native input resistance. The sample was biased for 10 min before X-ray exposure, apart from $W_{\pm}$ measurements immediately after bias application. The beam of X-rays was produced by a Dunlee PX1412CS tube with a DU-304 insert and a tungsten target. A 200 ms long, 60 kVp pulse of X-rays passed through 1.3 mm of Al filtration, which hardened the beam, and then was collimated by a 2 mm thick lead plate. The resulting poly-energetic X-ray beam incident on the detector has an average energy of ≈ 36 keV with energies ranging from 11 keV to 60 keV.

2.2.3 Experimental Setup - DC kinetics

DC kinetics was measured for various applied fields (F_0 = 5, 10, 15, and 20 V/μm), conventional for efficient detector operation. The experimental setup can be seen in Figure 2.2b, where a Stanford Research Systems PS350 power supply applies a positive bias to the ITO contact. A Keithley 35617EBS electrometer connected to the top Au contact measured the resultant DC. The electrometer and the power supply were controlled via a script executed on a control computer, connected by a GPIB interface (Tektronix AD007). The power supply was ramped to V_0 at 5 V/s to avoid large magnitude spikes in DC that could damage the detector. Once F_0 was achieved, the electrometer recorded the DC at a rate of 1 s^{-1} for two hours. After the DC recording period passed, the bias voltage ramped to 0 V at the same rate, and the detector was held in a resting configuration for 4 h. A 100 MΩ resistor in parallel with the detector ensured proper grounding during the resting period. The detector was installed within a light-tight box, which prevents any photogenerated

current, and allowed to rest in a short-circuit fashion for several hours before the experiment began to drain any previously trapped charge.

2.3 Results

2.3.1 Temporal Performance and Sensitivity Characterization

Figure 2.3 compares the photocurrents induced by continuous irradiation for 0.2 s and by modulated irradiation at 30 frames per second of the PI/a-PbO detector. The photocurrents are normalized to the steady-state magnitude of the continuous response. When the PI/a-PbO detector was exposed to continuous irradiation, it demonstrated a quasi-rectangular X-ray response. At the beginning of irradiation, the photocurrent increased almost instantly and remained at a nearly constant amplitude throughout the X-ray pulse duration. After the termination of the X-ray pulses, the amplitude rapidly fell back to the DC level. A slight increase in photocurrent at the start of the X-ray response is due to the characteristic overshoot of the X-ray flux rather than the detector's behavior, as verified by an identical response from a silicon photodiode.

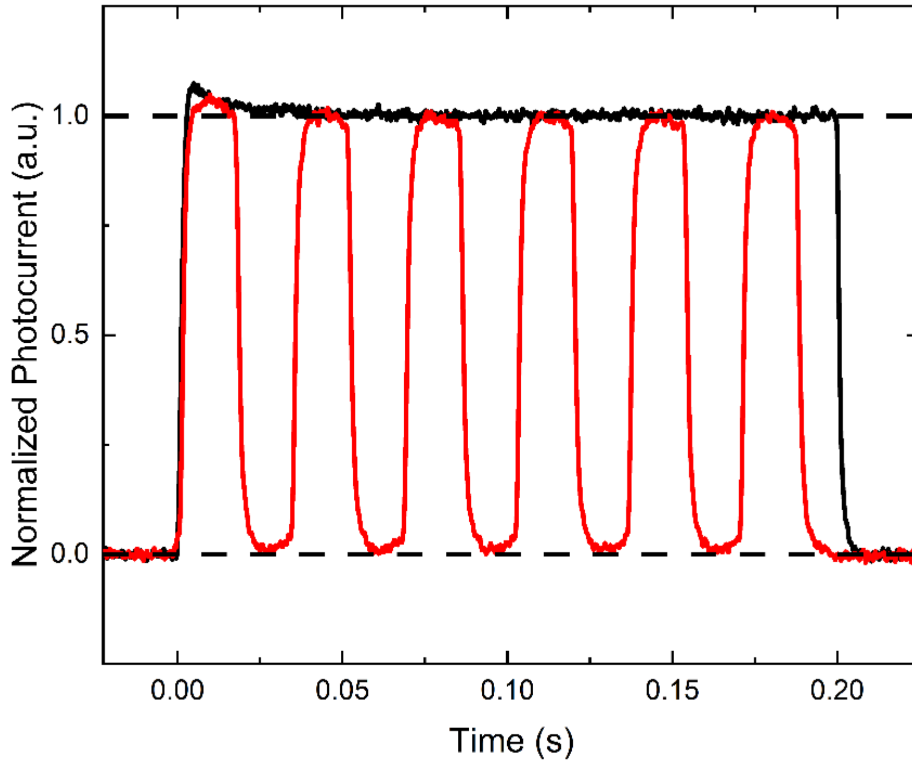

Figure 2.3. *The X-ray response of the PI/a-PbO detector, biased at 20 V/μm, to a continuous (black) and modulated (red) beam of X-rays. Modulated beam has a frame rate of 30 frames per second, matching that used in fluoroscopy. The photocurrent is normalized to the steady-state magnitude of the continuous response.*

The response of the PI/a-PbO detector to a series of short X-ray pulses with a rate of 30 frames per second indicates excellent temporal performance. During each frame, the photocurrent rises to the level of the continuous pulse response and remains there for the frame's duration. The response drops almost to the DC level when the frame ends. Lag values were calculated using the concept described in [7], [18], [26] and were found to be ~1%.

Figure 2.4 shows how ehp creation energy decreases with time after bias is applied. It was measured sequentially immediately after applying the bias (denoted in Figure 2.4 as $W_{\pm}^{inst.}$), with a short interval of 10 s between adjacent measurements. The obtained values were normalized to

the reference point, which is W± measured 10 min after applying the bias. Figure 2.4 presents only the measurements acquired during the first ~40 s after applying the bias and shows that initially, $W_{\pm}^{\text{inst.}}$ is ~30% greater than the reference point and approaches it over time.

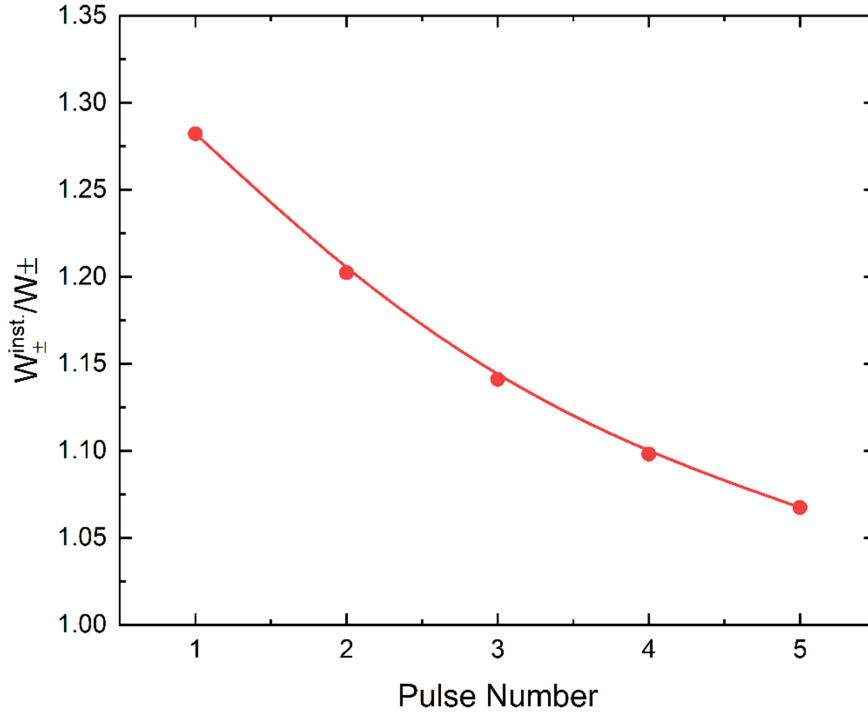

Figure 2.4. *The ratios of W± measured immediately after the application of the bias ($W_{\pm}^{inst.}$) to W± measured after waiting 10 minutes post bias application ($W_{\pm}^{inst.}/W_{\pm}$). Note that W±, measured 10 minutes after the bias was applied, was chosen as the reference point because it is observed that after this amount of waiting the ehp creation energy remains relatively constant, undergoing very little change over time.*

2.3.2 DC Kinetics

Figure 2.5 shows experimental DC kinetics data plotted in a semi-log scale at different fields. DC decays by almost two orders of magnitude post-bias application. At 10 V/μm, the most relevant field for direct conversion detector operation, DC magnitude is initially ≈26 pA/mm^2 and decays to ≈0.3 pA/mm^2 two hours after bias application. With an increased applied field, the

magnitude of DC increases. However, at all fields, DC decays below the operational threshold of 1 pA/mm^2 after two hours, as seen in Figure 2.5.

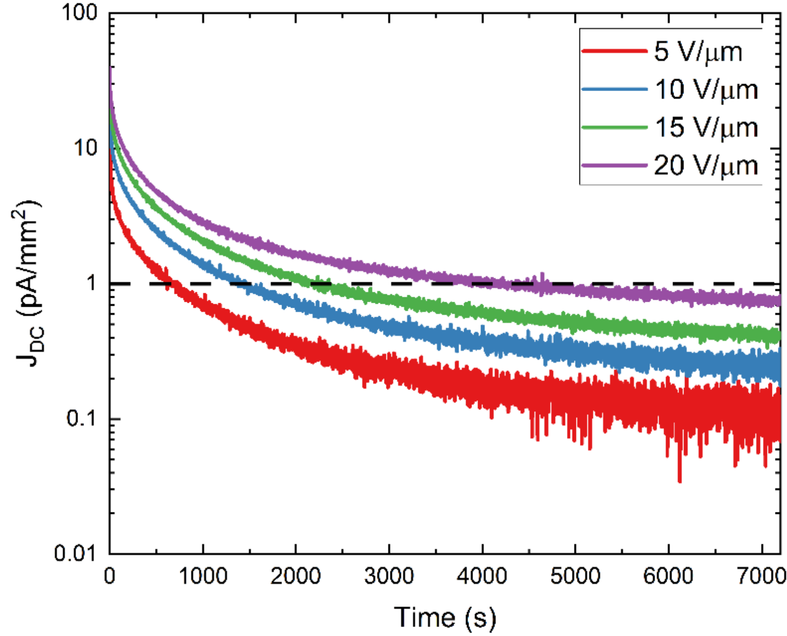

Figure 2.5. *Experimental DC kinetics data plotted in a semi-log scale corresponding to a PI/a-PbO detector biased at selected fields (5 – 20 V/μm) for two hours. The horizontal dashed line illustrates the operational threshold of 1 pA/mm^2. Data extracted from* [26].

2.3.3 Mathematical Model

A mathematical model was derived to probe the DC decay mechanisms present in the PI/a-PbO detector by simulating experimental kinetics data. Our model uses an approach developed in [30], [32], [33], [43] to simulate DC kinetics in a-Se blocking structures and extend it to account for the peculiarities of PI/a-PbO detectors. The model is based upon the following assumptions: (1) The primary source of DC in the PI/a-PbO detector is the injection of holes from the positively biased electrode proportional to the electric field at the electrode/PI interface. This is the case for a-Se detectors [30], [32], [43], which exhibit similar DC behavior compared to a-PbO-based

detectors. The assumption that injection is the primary source of DC is further fortified by the fact that the inclusion of a blocking layer, engineered to suppress injection, reduces DC significantly in a-PbO-based detectors. A secondary source of DC is the thermal generation and subsequent multiple-trapping (MT) controlled transport in the bulk of a-PbO. The injection and thermal generation of holes are exclusively considered as they are major carriers in PbO [49], [50]. (2) Injected holes are deeply trapped within the PI layer, which screens the applied electric field, a mechanism established for PI blocking layers in [43]. The resulting field redistribution within the detector structure occurs, causing the magnitude of the field at the ITO/PI interface to decrease, reducing injection and DC. (3) The concentration of deep trapping states within the a-PbO layer is negligible compared to that in PI [43], [55], and thus trapping in the bulk of a-PbO can be negated in terms of space charge accumulation that would contribute to the field redistribution.

The time-dependent electric displacement field redistribution and MT transport are illustrated in Figure 2.6, where $F_{PI}(x,t)$ and $F_{PbO}(t)$ are the electric fields within the PI and a-PbO layers, respectively; ε_0 is the vacuum permittivity, $\varepsilon_{r,PI}$ is the relative permittivity of PI, $\varepsilon_{r,PbO}$ is the relative permittivity of a-PbO, and E_V is the valence mobility edge of a-PbO. The exact expressions for $F_{PI}(x,t)$ and $F_{PbO}(t)$ will be discussed and derived later in the text (Equations (2.5) and (2.8)).

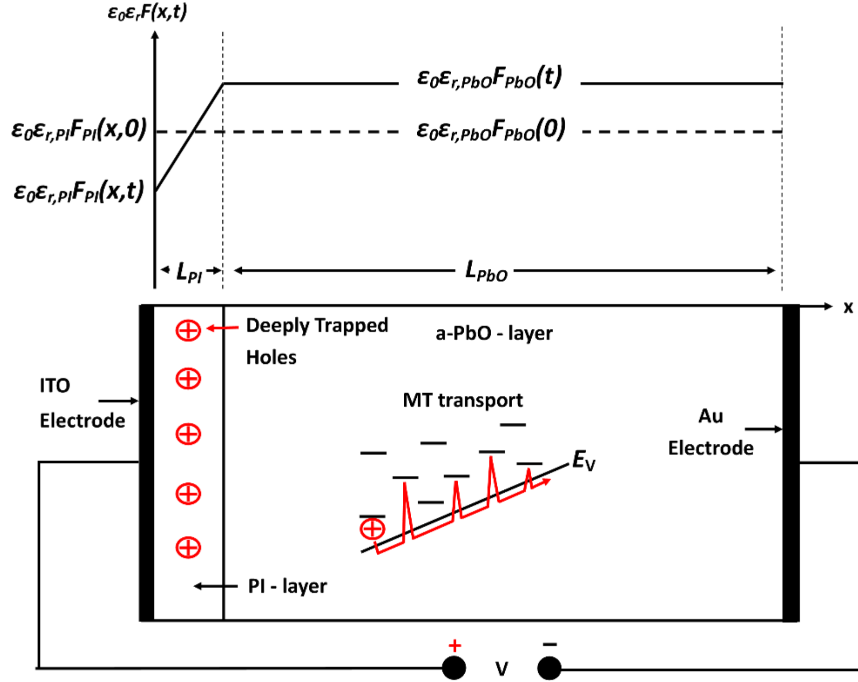

Figure 2.6. *A simplified schematic diagram of the PI/a-PbO detector and its time-dependent spatial electric displacement field profile. The dashed line represents the displacement field at the instant of bias application. The solid line represents the displacement field profile post-bias application when holes have accumulated in PI. In addition, a schematic of MT transport of thermally generated holes through the bulk of a-PbO is illustrated.*

In the model, holes undergo thermionic emission over a Schottky potential barrier, from the positively biased electrode (ITO) into the PI layer. The resulting current density of holes is described by:

$$J_h(t) = eN_v\mu_h F_{PI}(0,t)exp\left[\frac{-\left(\varphi_h - \beta_S\sqrt{F_{PI}(0,t)}\right)}{kT}\right], \tag{2.1}$$

where e is the elementary charge, N_v is the effective concentration of states in the valence band, μ_h is the effective hole mobility, φ_h is the energy barrier height experienced by holes in the

absence of an applied field, and kT is thermal energy, all pertaining to PI. In addition, β_S is the Schottky coefficient that is equal to $\sqrt{e^3/(4\pi\varepsilon_{r,PI}\varepsilon_0)}$.

The drift of the injected holes induces a current density of $J_h(t) = e\mu_h p(t) F_{PI}(0,t)$ where *p(t)* is the concentration of drifting holes. Therefore, the concentration of drifting holes near the ITO/PI interface is described by:

$$p(t) = N_v exp\left[\frac{-\left(\varphi_h - \beta_S\sqrt{F_{PI}(0,t)}\right)}{kT}\right]. \tag{2.2}$$

Drifting holes are then captured by energetically distributed localized states in PI. Trapped holes can be released after some time, proportional to an activation energy needed to escape, and be re-trapped into other unoccupied states. This model considers a uniform volume concentration of trapping states within the bulk of PI ($N_{\rho,m}$). The trapping levels have been segmented in *m* discrete energy depths within the bandgap of PI. The differential equations to describe the trapping rate of holes within the bulk of PI are:

$$\frac{d\rho_m(t)}{dt} = p(t)C_{t,m}\left[N_{\rho,m} - \rho_m(t)\right] - \frac{\rho_m(t)}{\tau_{r,m}}. \tag{2.3}$$

Here, $C_{t,m}$ is the deep trapping coefficient related to the trapping time constant (τ_c) by $C_{t,m} = 1/(N_{\rho,m}\tau_c)$ [56]. Additionally, $\tau_{r,m}$ is the release time constant, which is exponentially dependent on the activation energy ($E_{a,PI}$) needed for a hole to escape from a trap by:

$$\tau_{r,m} = \frac{1}{\omega_0}\exp\left[\frac{E_{a,PI}}{kT}\right], \tag{2.4}$$

where $1/\omega_0$ is the pre-exponential factor and ω_0 is usually assumed to be on the order of the phonon frequency. Without an electric field, the activation energy needed for a hole to escape from an individual trap in Equation (4) is equal to the energy or depth ($E_{\rho,m}$) of a trap. However, when

an electric field is applied, thermally assisted tunneling lowers the activation barrier for a hole to be released from the trap. As a result, $E_{a,PI}$ in equation 4 becomes smaller than the trap depth by $E_{a,PI} = E_{\rho,m} - \Delta E = E_{\rho,m} - e\beta F_{PI}(0,t)$, where β is proportional to the tunneling distance under the energy barrier [57]. As for the τ_c, it is treated as an electric field independent constant as a first-level approximation.

The instantaneous electric field at the ITO/PI interface is found by solving Poisson's equation in 1D cartesian coordinates, with the following boundary conditions: The integral of the electric field distribution must be equal to V_0, the potential is continuous at the PI/a-PbO interface, and the displacement electric field at the PI/a-PbO interface is continuous. Solving for the field at the ITO/PI interface, the following expression was obtained:

$$F_{PI}(0,t) = \frac{V_0}{\left(\frac{\varepsilon_{r,PI}}{\varepsilon_{r,PbO}} L_{PbO} + L_{PI}\right)} - \frac{e\rho(t)L_{PI}}{2\varepsilon_{r,PI}\varepsilon_0}\left(\frac{\varepsilon_{r,PbO}L_{PI} + 2\varepsilon_{r,PI}L_{PbO}}{\varepsilon_{r,PbO}L_{PI} + \varepsilon_{r,PI}L_{PbO}}\right) \tag{2.5}$$

$$\rho(t) = \sum_m \rho_m(t), \tag{2.6}$$

where $\rho(t)$ is the volume density of trapped holes within the bulk of PI. Here, as the density of trapped charge increases, the applied electric field is screened, and the field at the ITO/PI interface is lowered. As the field decreases at the interface, so does injection.

Another component of DC is the generation and transport of equilibrium holes in the bulk of a-PbO. Here we assume that holes drift through the bulk of a-PbO by MT mechanisms which is commonly considered in inorganic disordered semiconductors [57]. In the MT process, holes move only via extended states below the valence mobility edge. This motion is interrupted by the trapping of carriers into shallow localized states within the band tails and subsequently undergoes

field-assisted thermal release back into extended states [22]. To account for the transport mechanisms present in the MT regime, an effective temperature (T_{eff}) is introduced [22], given by:

$$T_{eff} = \left[T^2 + \left(\gamma \frac{eF_{PbO}(t)a}{k}\right)^2\right]^{1/2}. \tag{2.7}$$

In Equation (2.7), γ is a dimensionless coefficient and a is the localization length of trapping states in the band tail. The field within the bulk of a-PbO ($F_{PbO}(t)$) is similarly derived as $F_{PI}(x,t)$ was and is given by:

$$F_{PbO}(t) = \frac{V_0}{\left(\frac{\varepsilon_{r,PbO}}{\varepsilon_{r,PI}} L_{PI} + L_{PbO}\right)} + \frac{e\rho(t){L_{PI}}^2}{2\varepsilon_0(\varepsilon_{r,PbO}L_{PI} + \varepsilon_{r,PI}L_{PbO})} \tag{2.8}$$

In the MT transport regime, mobility is dependent on T_{eff}. The effective temperature-dependent hole mobility in a-PbO is described as:

$$\mu_{h,PbO}(T_{eff}) = \mu_0 exp\left[\frac{-E_{a,PbO}}{kT_{eff}}\right], \tag{2.9}$$

where $E_{a,PbO}$ is the average activation energy needed for a charge to escape from shallow localized states within the band tail.

To derive the current density induced by thermally generated holes, the concentration of drifting holes is found by solving the continuity equation for a uniform generation of holes throughout the bulk of a-PbO under steady-state conditions. Utilizing the solution to the continuity equation and $\mu_{h,PbO}(T_{eff})$, the current density is:

$$J_{th}(t) = e\mu_{h,PbO}(T_{eff})F_{PbO}(t)\tau_h g_h * \left[1 - \frac{\mu_{h,PbO}(T_{eff})F_{PbO}(t)\tau_h}{L_{PbO}}\left(1 - exp\left[\frac{-L_{PbO}}{\mu_{h,PbO}(T_{eff})F_{PbO}(t)\tau_h}\right]\right)\right]. \tag{2.10}$$

where τ_h is the hole lifetime and g_h is the thermal generation rate of holes in the bulk of a-PbO.

Thus, the total current density is:

$$J_{total}(t) = J_h(t) + J_{th}(t). \tag{2.11}$$

Field-dependent decay of DC was simulated by simultaneously solving the coupled first-order differential equations 3 numerically with Python. The model simplifies energetic disorder in PI by assuming three discrete trapping levels in the bulk of PI (see Table 2.1). Three levels are chosen as a first-level approximation, using the lowest number of levels that still accurately simulates the data. The range of trapping depths corresponds to previously reported results for PI [55]. The effective mobility of holes in PI is μ_h = 1x10^{-6} cm^2 / (Vs) [43], and the density of states within the valence band of PI is $N_v = 6 \times 10^{21}$ cm^{-3} [43]. A typical phonon frequency was used equal to $\omega_0 = 1 \times 10^{12}\ s^{-1}$ [33], [34]. Other parameters such as the bulk concentrations of trapping states ($N_{\rho,m}$) and intrinsic barrier height (φ_h) are deposition dependent and therefore are treated as fitting parameters. g_h, τ_c, and β are additionally treated as fitting parameters.

Table 2.1. *Parameters and their sources, utilized within the mathematical model in this investigation.*

Parameter	Value	Source
μ_h	1x10^{-6} cm^{2}V^{-1}s^{-1}	[43]
$\varepsilon_{r,PI}$	3.3	[46], Dark CELIV
$\varepsilon_{r,PbO}$	26	Dark CELIV
β	0.5 nm	Fitting Parameter
τ_c	9x10^{-4} s	Fitting Parameter
N_v	6x10^{21} cm^{-3}	[43]
ω_0	1x10^{12} s^{-1}	[33], [34]

g_h	2.32x10^{11} cm^{-3}s^{-1}	Fitting parameters based on [58], [59]
$E_{\rho,m=1}$, $E_{\rho,m=2}$, $E_{\rho,m=3}$	0.82, 0.86, 1.0 eV	[43], [55]
$N_{\rho,m=1}$, $N_{\rho,m=2}$, $N_{\rho,m=3}$	1x10^{18}, 1x10^{17}, 2.8x10^{16} cm^{-3}	Fitting Parameter
Φ_h	0.81 eV	Fitting Parameter
τ_h	1.8x10^{-6} s	[18]
γ	0.6	[22]
a	0.56 nm	[22]
$E_{a,PbO}$	0.5 eV	[22]

The relative dielectric permittivity of a-PbO and PI were determined by capacitance measurements through charge extraction by linearly increasing voltage (CELIV) without photoexcitation, i.e., dark-CELIV. Details pertaining to the technique of CELIV can be found in [13], [49], [50]. The dielectric permittivity of PI ($\varepsilon_{r,PI} = 3.3$) and a-PbO ($\varepsilon_{r,PbO} = 26$) was found. Measurements corresponded perfectly with manufacturer-specified dielectric permittivity of PI [46].

All parameters used in the model are shown in Table 2.1, and the simulation results can be seen in Figure 2.7 as dashed red lines. The simulated DC is broken into injected (dashed-dotted green lines) and thermally generated (blue lines) components. The model was simultaneously simulated four different kinetics data corresponding to different applied fields. Meaning that all the fitting parameters are held constant throughout different applied fields, leaving only the parameter V_0 to vary between them. Simultaneously fitting all four experimental data was

deliberately chosen to adhere to physical accuracy since the parameters $N_{\rho,m}$, Φ_h, τ_c, β, and g_h in the PI/a-PbO detector have no dependence on the applied bias. As a result of fitting all four applied fields simultaneously, the fitting was guided by the overall average quality of fitting of all four datasets rather than the quality of fitting for each applied field individually. Overall, the fitting most accurately represents the experimental data (black lines) at higher applied fields of 15 and 20 V/μm, while accuracy decreased with decreasing applied fields. Generally, fitting is least accurate at short times, and as the simulation evolves, the fitting becomes more accurate. For each applied field, the initial DC due to hole injection is much larger than that due to thermally generated holes. As the field undergoes a redistribution, injection decreases until thermal generation becomes dominant, except for 20 V/μm.

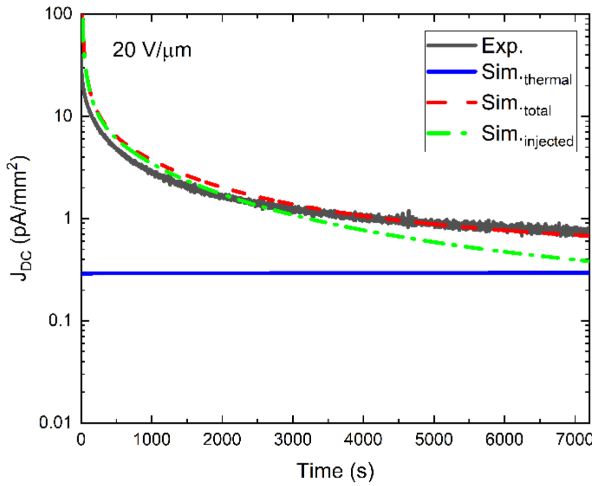

(**a**)

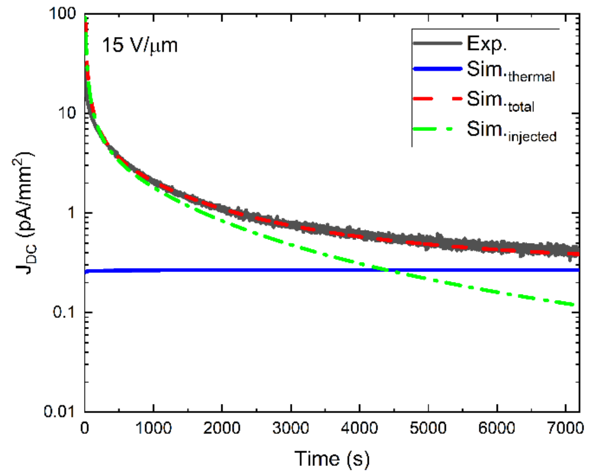

(**b**)

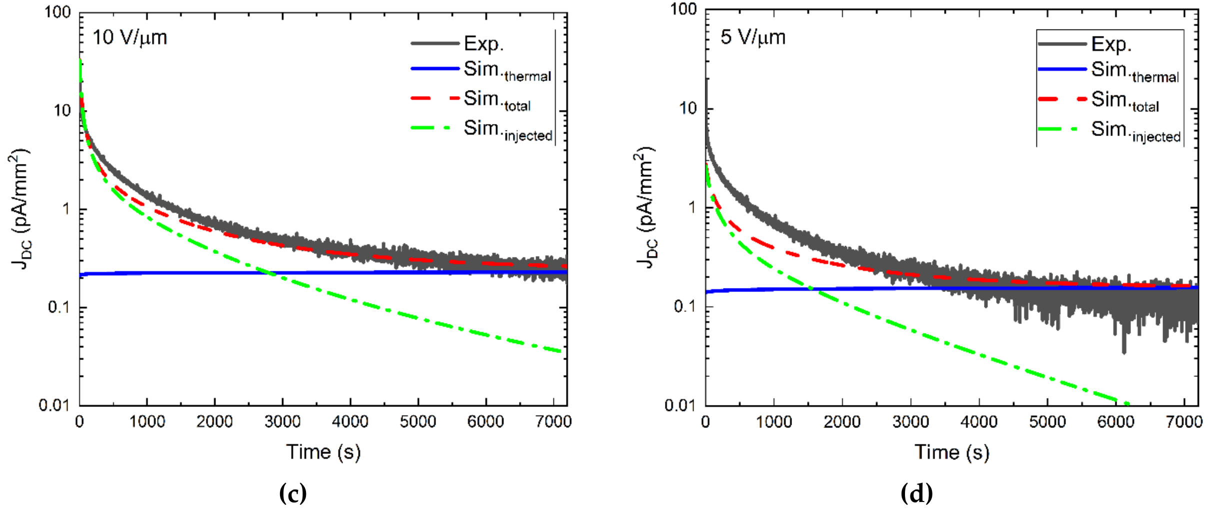

Figure 2.7. *Experimental (solid black) and simulated (injected (dash-dotted green), thermal (solid blue), and total (dashed red)) DC kinetics data plotted in a semi-log scale corresponding to a PI/a-PbO detector biased at fields of a) 20 V/µm, b) 15 V/µm, c) 10 V/µm, and d) 5 V/µm for two hours.*

2.4 Discussion

The experimental results demonstrate that the DC in the evaluated single-pixel PI/a-PbO prototype detector is a function of the applied bias and time: it decays with time from the instant of application of the nominal voltage and settles at low steady-state values. The steady-state value of DC depends on the applied voltage; however, for voltages relevant to the operation of the direct conversion flat-panel X-ray imagers (10–20 V/mm), it does not exceed 1 pA/mm^2. This value lies in the low end of acceptable DC levels that is often quoted to be between 1 to 10 pA/mm^2, depending on the exact application [2], [60]. It is important to note that even at the highest applied field, tested here (20 V/µm), the DC in the presented PI/a-PbO detector prototype is on the same order of magnitude as in multilayer a-Se-based detectors at the same nominal applied field [39], [43], [48], [61]. This suggests the possibility of using a higher field (i.e., $10 < F_0 \leq 20$ V/µm rather than the 10 V/µm used in a-Se detectors) to improve charge collection and $W_{\pm}$ while keeping DC at tolerable levels. In turn, the thickness of the PI layer should be optimized for operation at 20 V/µm. “Optimizing” means that the blocking layer should have adequate thickness to reduce the

DC but not too thick so that a substantial fraction of the applied voltage drops over it rather than the photoconductor, as previously shown in [43]. This reduces the field inside the photoconductor, negatively affecting charge collection efficiency and the temporal performance of the detector.

Qualitatively, the mechanism of DC decay can be explained by deep charge carrier trapping and polarization effects that cause the instantaneous electric field at the ITO/PI interface to decrease and increase within the bulk of a-PbO. As a result, we achieve two very useful effects: on the one hand, the DC decreases, and on the other hand, the collection efficiency of X-ray generated charge is improved, and $W_{\pm}$ decreases (since it is field-dependent [7], [12]). This is shown in Figure 2.4, where $W_{\pm}$ decreases after the instant of bias application. We visualize the field redistribution within the PI/a-PbO detector in Figure 2.8 where the electric displacement field ($D(t) = \varepsilon_0 \varepsilon_r F(t)$) profile throughout the PI/a-PbO detector structure is plotted as a function of time for an applied electric field of 20 V/µm. The *D* profile is displayed in Figure 2.8 as the electric field profile is discontinuous at the PI/a-PbO interface due to the difference in the dielectric permittivity of PI and a-PbO. To avoid this discontinuity that would complicate visual interpretation, *D*, which is continuous, is displayed.

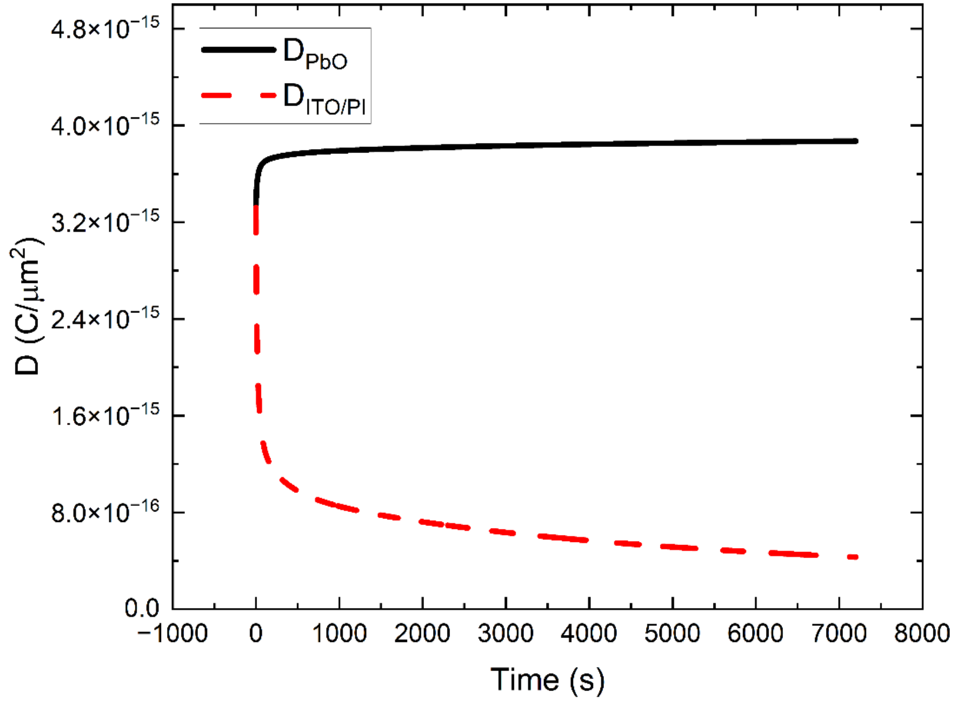

Figure 2.8. *Electric displacement field (D(t)) at the ITO/PI interface (dashed red) and throughout the bulk of a-PbO (solid black) as functions of time for an applied field of 20 V/μm.*

For a quantitative analysis of the bias-dependent transient DC, we assume that trapping occurs within the PI blocking layer itself. Of course, localized states have continuous distribution (most probably, an exponential density of states (DOS) typical for organic disordered materials). However, since the DOS is unknown, we replace it with a set of three discrete levels in the bulk (where the lower concentration of states corresponds to deeper centers). Despite the simplification, our model allows us to understand how much net space charge due to trapped carriers (e.g., holes) is needed to modify the internal field and to limit the injection of holes from the ITO electrode.

Numerical calculations show that within the simplifications of the presented model, it is impossible to find such a set of fitting parameters that provides a precise description of the experimental data in the entire time range tested here for all applied fields simultaneously. One can see from Figure 2.7 that the dashed red line perfectly agrees with experimental data at times

near the end of the testing period but deviates from it at times shortly after bias application. Interestingly, the degrading quality of fitting in the initial time interval was also observed in [30], [33], where simulated DC kinetics have been fitted to experimental kinetics at varying applied fields for an *n-i-p* a-Se detector. The good agreement between experimentally measured and simulated results at times when the DC decay begins to saturate is not surprising since it is ultimately the total amount of trapped charge, regardless of the mechanism of its trapping and distribution over localized states, that determines the steady-state DC. The situation is directly opposite at the initial stage of the field application when it is the probability and capture rate, the possible subsequent release of the trapped charge, and its redistribution over various energetically distributed localized states that determine the kinetics of DC. Although in our modeling, we made a step forward (in comparison to previous works on a-Se) to account for a field-assisted release from deep traps in the PI layer, the observed discrepancy between simulated and experimental results where experimental DC decays at a different rate than the simulated one suggests that there is an additional mechanism that affects the kinetics of the electric field redistribution, and it escapes our attention. Below we consider the hopping exchange of carriers between the traps and show how taking this effect into account improves the quality of the simulation even with a simplified energetic disorder in the bulk of PI, which assumes only three discrete deep trapping levels.

As was shown in [57], the release of charge from traps by thermally assisted tunneling can be further enhanced by field-assisted hopping transition from a given trap to a shallower surrounding trap. Since this process makes it easier for a hole to be activated to the valence band, the release times $\tau_{r,m}$ become shorter. In addition to the strength of the electric field, two factors influence the impact of this effect: the depth of a trap and the parameter $N_{\rho,m}a^3$ [57]. For first-order approximations for these numbers, we used data from Table 1 and estimated $N_{\rho,m}a^3$ to vary

from 0.005 for the deepest trap of 1.0 eV ($m = 3$) to 0.18 for the shallowest trap of 0.82 eV ($m = 1$). The enhancement factor for the release of carriers from traps is defined as the ratio between the mean release time from a single trap and the release time from the same trap in the presence of a nearby trap at the optimal position [57]. This factor varies from ~2 for the shallowest trap at the weakest nominal field of 5 V/μm to ~9 for the deepest trap of 1.0 eV at the strongest nominal field of 20 V/μm. These estimations suggest that we should not neglect that a hole's release from a trap to the valence band can be substantially enhanced by the presence of an additional, shallower trap. The hopping exchange of carriers between traps also provides additional channels for the capture of a hole from the valence band to a particular trap that leads to enhancement of the capture rate for a given trap [57]. Although the above considerations suggest that both τ_c and $\tau_{r,m}$ should be electric field-dependent, without knowing the exact concentrations and energy distribution of the localized states as well as the localization length and effective mass of carriers within these localized states, it is difficult for us to derive analytic equations describing the field-enhancement on the de-trapping process and the influence of the field on the capture probability. Instead, Equations (2.1)–(2.11) are left unmodified, and we let τ_c vary with the applied electric field and β, and therefore $\tau_{r,m}$, vary with trapping level depth within the band tail of PI. The field dependencies of τ_c and $\tau_{r,m}$ are derived from the best fit between the calculated and experimentally measured DC kinetics. The results are shown in Figures 2.9–2.11.

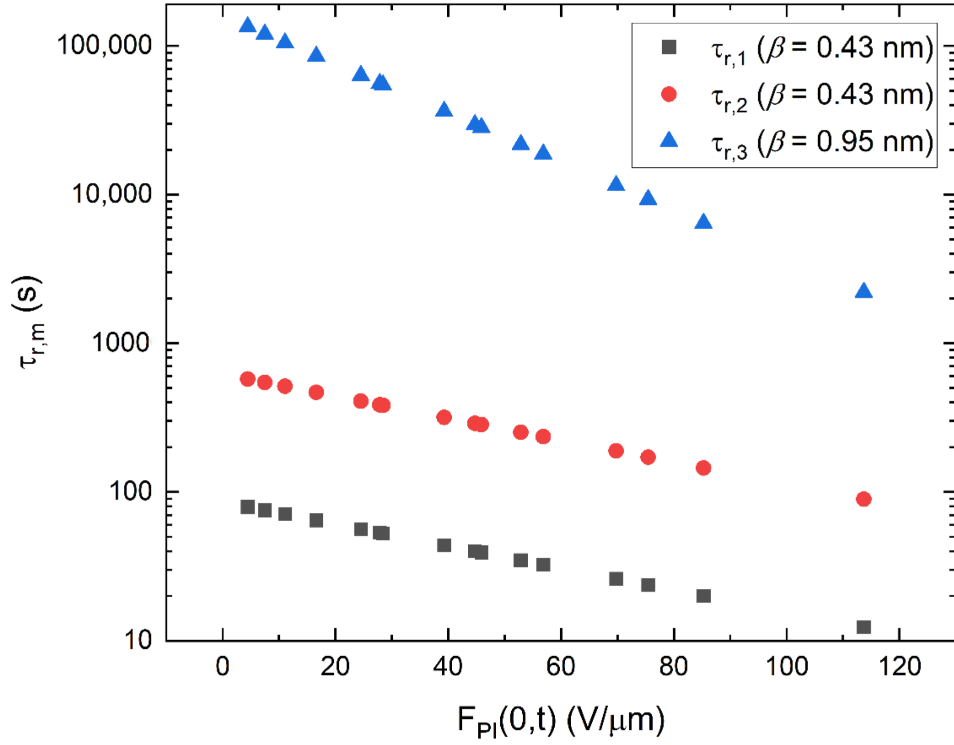

Figure 2.9. *Release time ($\tau_{r,m}$) plotted as a function of the instantaneous field at the ITO/PI interface ($F_{PI}(0,t)$). For the deepest level of traps at 1.0 eV ($\tau_{r,3}$), a stronger field dependence, compared to other levels, yielded a more accurate fit between experimental and simulated data.*

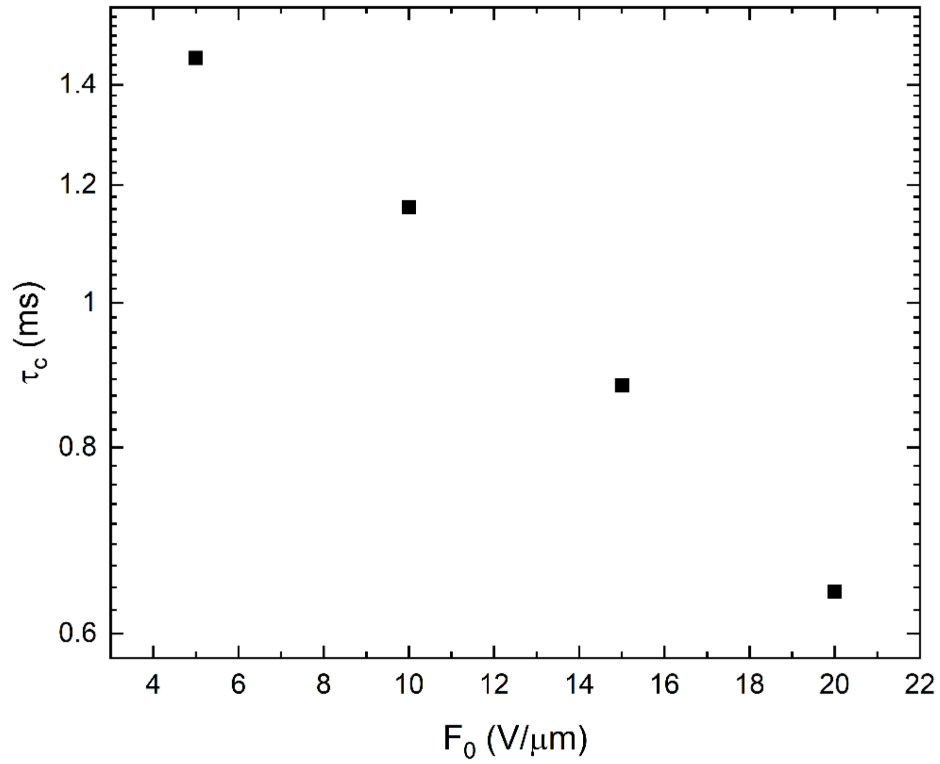

Figure 2.10. *Capture time (τ_c) as a function of the applied nominal field (F_0). A unique constant τ_c was given for each applied nominal field to obtain the best fitting between experimental and simulated data.*

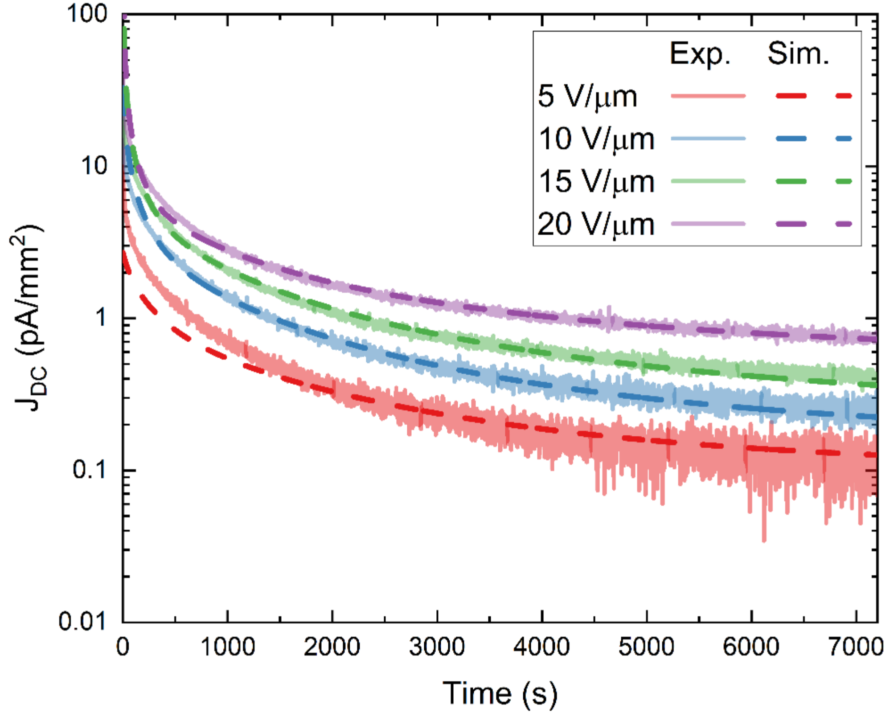

Figure 2.11. *Simulated (dashed lines) and experimental (solid lines) DC kinetics data plotted in a semi-log scale corresponding to a PI/a-PbO detector biased at selected fields (5-20 V/µm) for two hours. Here the model is modified by treating the release times ($\tau_{r,m}$) and capture times (τ_c) as electric field dependent parameters in accordance with the hopping enhanced release and capture mechanisms discussed above.*

Figure 2.9 shows the release times for the three discrete levels of traps with the energy depths of 0.82 eV, 0.86 eV, and 1 eV considered in our model. Much steeper field dependence for the deepest trap suggests that the release rate from this trap is enhanced by the presence of other (shallower) traps in full agreement with a model presented in [57]. This effect is accompanied by the equal enhancement of the capture time for the deepest trap due to the assistance of the surrounding traps. The dependence of such an enhancement on capture time is shown in Figure 2.10.

Figure 2.11 presents a comparison between experimental (solid lines) and simulated (dashed lines) DC kinetics data, modified to account for the hopping-assisted release of charge

carriers from trapping sites. Much better agreement between the experimental and simulated results is evident when compared to Figure 2.7 (a 33.6% reduction in the total cumulative residual sum of squares (RSS) of all four applied fields).

It is also useful to examine the simulated kinetics of trap occupancy (Figure 2.12). Holes trapped within deep sites are effectively lost to conduction as the release time for these traps is longer than the duration of DC decay measurements. The other shallower levels (0.82 and 0.86 eV) play a role in decay, but holes trapped in these levels are released during the time frame of DC decay and then are lost to the deepest traps. Therefore, the major contribution to the creation of this positive space-charge barrier is made by charge trapped in the deepest traps (1 eV).

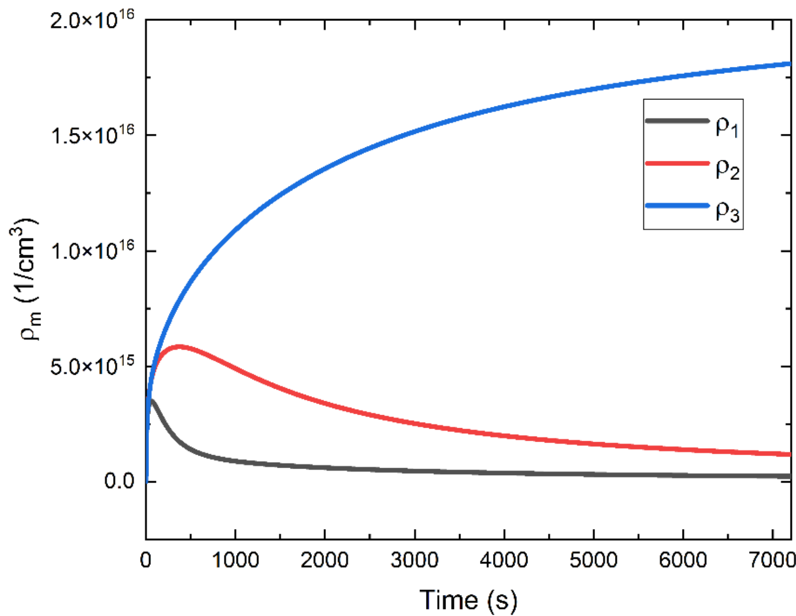

Figure 2.12. *The occupancy of trapping sites, segmented into three discrete levels, plotted as a function of time. Here, this data is obtained from the simulated kinetics corresponding to a nominal field of 20 V/μm. Note that this data is simulated from the unmodified model, where hopping assisted release and capture is not accounted for.*

The total concentration of the deepest traps within a thickness of 1.1 mm of PI used here seems optimal when 10 V/mm is utilized as a nominal operating electric field. Indeed, this is seen in Figure 2.7; at 10 V/mm, the steady-state DC is dominated by thermal generation, not injection. However, a thicker layer of PI may be desired for larger electric fields to reduce the DC to a limit determined by thermal generation. Based on our simulated results, at 20 V/mm, this can be achieved with a PI layer thickness of 1.3 μm.

As previously mentioned, when introducing a foreign material (PI) into the structure of a direct conversion detector, the fear that states are created at the interface of the photoconductor and the foreign material is always present. During the model's derivation, trapping states at the interface of PI and a-PbO have been included in previous iterations. However, the delineation between surface trapping and bulk trapping in PI does not change the fitting quality. The experimentally measured decay can be explained by the trapping in the bulk of PI alone. This indicates that the concentration of states at the interface is negligible compared to that in the bulk of PI.

Evaluation of temporal response to X-ray irradiation in the PI/a-PbO detector was very important to demonstrate that while suppressing DC to acceptable levels, the presence of the PI blocking layer does not degrade the performance of the PI/a-PbO detector. As can be seen in Figure 2.3, the amplitude of the response to a continuous beam of X-rays stays constant during irradiation, confirming three findings: (1) The steady-state redistribution of the electric field that is responsible for bias-dependent DC behavior is unaffected by the presence of the photogenerated charge. (2) Photogenerated charge does not experience deep trapping at the PI/a-PbO interface during the drift through the PI layer. (3) There is no X-ray-triggered injection occurring in the detector.

During irradiation of the PI/a-PbO detector to a modulated beam of X-rays, the photocurrent within each frame and the amplitude of successive frames remain constant. This contrasts with similar PI/a-Se detectors, whose photo-response to a beam of modulated X-rays exhibits unstable temporal response. The photo-response shown in [43] demonstrates that the photocurrent during each frame decreases over time. This behavior is attributed to the accumulation of photogenerated electrons at the PI/a-Se interface that temporarily degrades the internal electric field, restored via injection before the next frame begins [43]. In another publication, pertaining to a PI/a-Se detector, the amplitude in each successive frame is shifted up. This behavior is caused by a rise in the DC level, speculated to result from increased injection triggered by the trapping of X-ray-generated electrons at the interface [48]. The response seen in Figure 2.3 indicates that the PI/a-PbO detector lacks these imperfections (i.e., interface states that trap photogenerated electrons), causing unstable temporal X-ray response in PI/a-Se detectors. Overall, the PI/a-PbO detector's response to continuous and modulated X-ray pulses confirms that PI does not degrade temporal performance or charge collection efficiency.

2.5 Conclusions

This investigation reports on the temporal performance, sensitivity, and DC behavior of a PI/a-PbO detector. Characterization of temporal performance shows that it is unhindered by the inclusion of a PI layer, and the detector exhibits a lag of ~1% at 30 Hz and 20 V/µm. DC kinetics shows that at every field reported here (5–20 V/µm), a PI layer thickness of 1.1 µm was sufficient to cause DC to decay below the 1 pA/mm^2 operational threshold. This reveals that PI is a practical approach to suppress DC in a-PbO-based direct conversion detectors. If necessary, the DC can be further reduced by simply increasing the thickness of the PI layer. Increasing the thickness of the PI layer will increase the total number of deep trapping centers that can accumulate space charge

to suppress carrier injection further and stabilize the DC at the fundamental limit determined by thermal generation, even at large applied fields.

In order to explain the experimentally measured DC decay in the PI/a-PbO detector, in the entire range of electric fields accessed in this work, we modified a 'standard' mathematical model used to simulate DC kinetics derived by others [6,15,24,25] to account for hopping-assisted release and capture of holes with filed-dependent trapping and release time constants. A noticeable improvement in the quality of fitting with the modified model, in comparison with a standard model, indicates that hopping transitions of trapped holes between localized states in the band tail substantially influences both the field-induced hole release and trapping. Both mechanisms play essential roles in reaching a steady-state occupancy level of different traps in the bulk of PI, resulting in a particular profile of the internal electric field.

In addition to the above theoretical considerations, our results suggest three practical results. First, a basic set of algebraic equations can be applied to find the numerical solution to the kinetics of electric field evolution that includes a realistic process of charge trapping. Secondly, the model can be used to approximate the optimal PI thickness for future iterations of a-PbO-based detectors without the need for time- and labor-intensive experimental trial and error. This can be applied to direct conversion detectors based on other photoconductors interfaced with PI by modifying the presented model to account for the particularities of the photoconductor. Finally, sensitivity measurements presented here revealed that a field redistribution and subsequent field increase within the a-PbO layer improves the detector's photogenerated charge collection efficiency and temporal performance. This can be implemented as a warm-up time, a common requirement of sophisticated electronics, for a-PbO-based detectors to improve SNR. Overall,

comprehending DC mechanisms of direct conversion detectors utilizing foreign material blocking layers, such as PI, gives essential insight into improving and optimizing their development.

Author Contributions: Conceptualization, T.T., and A.R.; methodology, T.T and O.G; software, T.T.; validation, T.T., O.G. and E.P.; formal analysis, T.T., O.G. and E.P.; investigation, T.T., O.G. E.P. and A.R.; writing—original draft preparation, T.T.; writing—review and editing, T.T., O.G. and A.R.; visualization, T.T; supervision, A.R.; project administration, O.G. and A.R.; funding acquisition, A.R. All authors have read and agreed to the published version of the manuscript.

Funding: Research was funded by Teledyne DALSA, the Natural Sciences and Engineering Research Council (NSERC), the Ontario Research Fund – Research Excellence (ORF-RE), and MITACS programs. The APC was funded by NSERC.

Institutional Review Board Statement: Not applicable.

Informed Consent Statement: Not applicable.

Data Availability Statement: The data presented in this study are available on request from the corresponding author.

Acknowledgments: The authors are thankful to Dr. Attila Csík for obtaining SEM image and to Dr. Gytis Juska and Dr. Sandor Kokineshi for stimulating scientific discussions.

Conflicts of Interest: The authors declare no conflict of interest.

Chapter 3: Conclusions

The research performed within this thesis is of both fundamental and practical importance. The fundamental scientific significance of the work is that our understanding of the properties of a-PbO is still incomplete (the complexity of amorphous semiconductors is known to tax solid state physicists). The presented results provided experimental evidence that allows us to test a new theory suggesting that in disordered materials the release of the trapped charge carriers above the mobility edge can be substantially enhanced by hopping between the traps. The practical significance of the photoconductor materials related research is that it helps to determine an optimal design and develop special blocking and multilayer PbO detector structures, that will withstand the high electric fields needed for high X-ray-to-charge conversion gain. Our industry partner, Teledyne DALSA, a Canadian and a global leader in digital imaging products and solutions for medical and industrial imaging markets, is dependent upon this information for their detector development and manufacturing projects. Teledyne DALSA recognizes the high potential of the application of a-PbO as an X-ray-to-charge transducer in the next generation of DALSA's direct conversion flat panel X-ray imaging detectors. A research agreement between Lakehead University and Teledyne DALSA was signed and outlines joint research opportunities, as well as knowledge and technology transfer for commercialization of a-PbO based detectors.

Below we summarize the main performance characteristics of a-PbO blocking structures which were improved or analyzed in this thesis.

3.1 PI/a-PbO Detector Temporal Performance

Temporal characterization results displayed in Figure 2.3 indicate that the inclusion of PI into the structure of an a-PbO-base detector does not degrade performance. Signal lag was calculated with the methodology described in [7], [18], [26], and Appendix A. Lag is larger at

lower applied fields, as shown in [26]; therefore, it was measured at F_0 = 10 V/µm (that is an operational electric filed in a-Se detectors) and at F_0 = 20 V/µm (that is a desired electric field in PI/a-PbO detectors for improved charge collection). When the PI/a-PbO detector is biased at F_0 = 20 V/µm and exposed to a beam of X-rays modulated by a rotating copper chopper at 30 Hz, the lag was found to be ~1%. This is less than the 5% signal lag exhibited by CsI detectors currently utilized for fluoroscopy [16]. However, even when lag is measured at F_0 = 10 V/µm, it is only slightly larger at ~3% and remains lower than that in commercial CsI detectors. These results indicate that the use of the PI layer to improve a-PbO blocking characteristic does not degrade detector time performance and is a plausible approach for real-time dynamic or multi-frame applications.

3.2 Dark Current Decay

At all applied fields evaluated in this investigation (5-20 V/µm), DC is initially high at the instant of bias application but decays by approximately two orders of magnitude below 1 pA/mm^2 within two hours. Of course, the magnitude of DC increases with increasing applied fields; however, even at F_0 = 20 V/µm, DC comes to a steady-state magnitude below 1 pA/mm^2, often stated as the low-end of the tolerable DC levels for direct conversion detectors [2], [26]. Therefore, for the a-PbO-based detector investigated here, 1.1 µm of PI is sufficient to suppress DC to tolerable levels at all fields tested. As a result of DC decaying below 1 pA/mm^2 even at the highest applied field means that the operation of PI/a-PbO detectors at applied fields greater than 10 V/µm ($10 < F \leq 20$) is achievable. Utilizing a larger applied field has the benefit of improving temporal performance [26] and X-ray sensitivity [12].

If it is desirable to integrate PI/a-PbO blocking structures into lower noise imaging array technology, such as CMOS or lower noise TFT, the model can give insight. The simulated results

in Figure 2.7 indicated that the thickness of PI is sufficient to suppress DC below tolerable levels, however, it could be further increased to lower DC further. PI acts to suppress injection to decrease DC, however, PI does not affect thermal excitation rate which determines the lowest attainable DC level. 1.1 μm of PI is sufficient to suppress injection below the level of thermal generation in the presented PI/a-PbO, only up to 15 V/μm. At an applied field of 20 V/μm, injection is not suppressed below the thermal generation level. Our simulations show that the optimal thickness of PI is 1.3 μm. Optimal refers to a minimum thickness that suppresses injection below thermal excitation. It is important to note that increasing the thickness of PI beyond the optimal thickness would not decrease DC further and more of the applied voltage would drop over the PI rather than the a-PbO layer.

This model can be used to find the optimal thickness of PI for future iterations of a-PbO-based detectors without time- and labour-intensive trial and error. By simply adjusting the thickness of PI in the model, a first approximation of the optimal thickness can be found easily. Additionally, by modifying the model to account for the peculiarities of detectors based on other photoconductors (utilizing the appropriate constants), it can be used to find the optimal thickness of PI for them. Making this model a powerful research and development tool for direct conversion detectors.

3.2.1 Mechanism of Dark Current Decay

The research within this thesis refined and enriched a 'standard' model of DC kinetics that is caused by a gradual electric field redistribution due to the accumulation of trapped charge within the blocking layers. This model was first developed for a-Se *n-i*, *p-i-n,* and PI blocking structures [30], [32], [33], [43] and then extended to our PI/a-PbO blocking structure. The trapped charge screens the electric field reducing it at the ITO/PI interface, suppressing injection and thus DC.

We demonstrate that modification of the 'standard' model to account for realistic mechanisms [57] of hopping transition-assisted trapping and release of holes within the PI layer greatly improves the quality of fitting between simulated and experimental decays. A better fitting quality indicates that hopping transitions are an important process determining the rate at which a steady-state occupancy of localized states within PI is reached.

3.2.2 Electric Field Redistribution

In addition to the internal field redistribution being responsible for the decay of DC, it also causes the field within the a-PbO layer increases over time, as visualized in Figure 2.8. This improves the detector's X-ray sensitivity and temporal performance. Indeed, X-ray sensitivity is experimentally shown (Figure 2.4) to improve as time progresses from the instant of bias application. X-ray sensitivity is inversely expressed as $W_{\pm}$ calculated according to methods explained in [12] and Appendix B. The electric field redistribution can be implemented as a warm-up time for a commercial PI/a-PbO detector, a common requirement for sophisticated electronics, that will improve SNR and temporal performance.

3.3 Future Work and its Significance

At the current stage of a-PbO detector technology development, PI/a-PbO/poly-PbO detector prototypes show immense promise for application in direct conversion X-ray medical imaging PI/a-PbO/poly-PbO detectors demonstrated low DC which offers higher X-ray sensitivity and lower radiation dose required to acquire a radiographic image. However, on an industrial scale the multilayer preparation procedure is still immature. The future work includes:

1. To scale-up multilayer PbO technology and to manufacture the first laboratory prototype of multi-pixel large-area (30×30 cm^2) flat-panel direct conversion imaging detectors where an X-ray photoconductive multilayer structure is deposited directly on imaging electronics.
2. To evaluate imaging performance of large area detector prototype at low exposure rates.

If successful, implementation of the developed PI/a-PbO/poly-PbO technology in commercial detectors has a potential to advance the radiation medical imaging field beyond the current standard of care. The replacement of existing imaging detectors with more sensitive and therefore safer alternatives will enhance the capabilities of clinically important imaging applications. It will enable the widespread adoption of Digital Breast Tomosynthesis (DBT) in the clinic and replace conventional X-ray fluoroscopy, which delivers a higher dose of radiation and whose capabilities are limited for cardiac intervention. Although highly innovative, PI/a-PbO/poly-PbO technology will be compatible with imaging devices currently in use, thereby maximizing the economic value and market potential of the research within this thesis.

Appendix A. Lag Calculations

The ratio of the photocurrent after the termination of the frame n (I_{photo}OFF) to the signal during the frame n (I_{photo}ON) is used to calculate signal lag. The DC level is subtracted from each photocurrent to account for its offset. The photocurrent during and after each frame is visualized in **Figure A.1**.

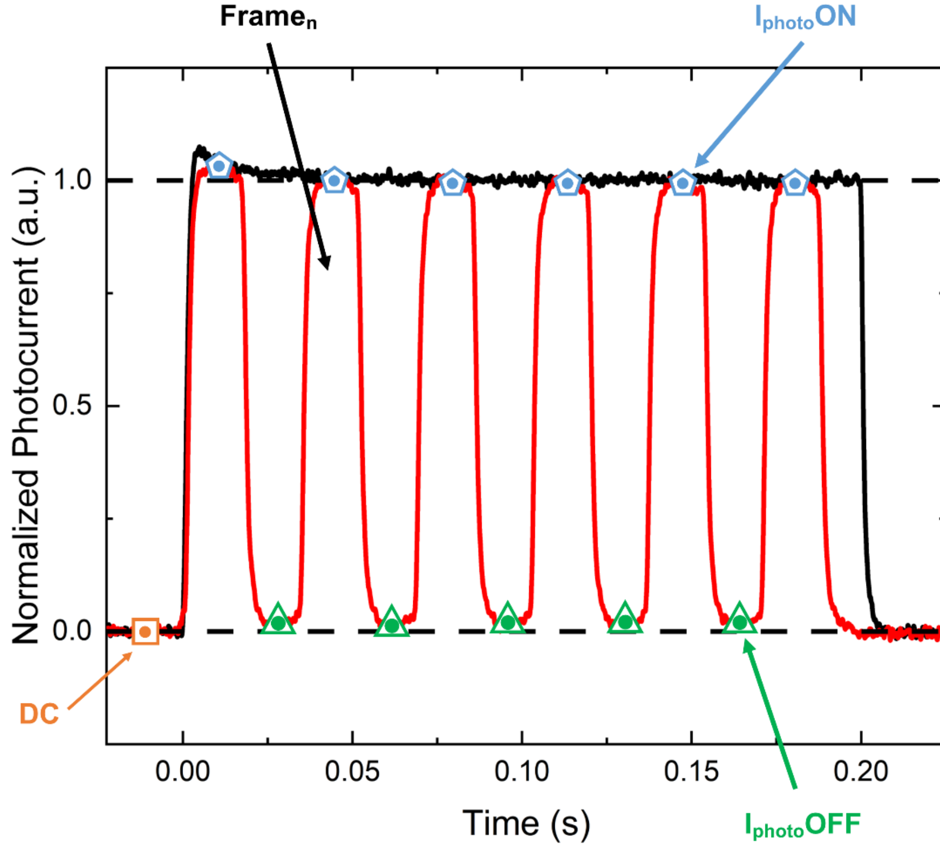

Figure A.1. *The X-ray response of the PI/a-PbO detector to a beam of continuous and modulated beam of X-rays with relevant values indicated for each frame.*

The lag of each frame is calculated with:

$$lag_n = \frac{I_{photo}OFF_n - DC}{I_{photo}ON_n - DC}. \tag{A.1}$$

The average lag for all the frames in the waveform is calculated by

$$\text{Average } lag = \frac{\sum_n lag_n}{n} \tag{A.2}$$

Appendix B. X-ray Sensitivity Calculations

X-ray sensitivity is inversely expressed as the work required to create on detectable EHP $W_{\pm}$. $W_{\pm}$ is expressed by:

$$W_{\pm} = \frac{E_{abs}}{N_{EHP}}, \tag{B.1}$$

where E_{abs} is the amount of energy absorbed by the detector and N_{EHP} is the number of EHP collected. N_{EHP} is calculated by integrating the photo-response recorded experimentally:

$$N_{EHP} = \frac{\int I_{photo} dt}{e}. \tag{B.2}$$

E_{abs} is calculated by considering the attenuation of an X-ray beam, simulated using a program developed in Python, passing through the PI/a-PbO detector. The program considers a beam of poly-energetic X-rays incident on the detector. The spectrum is simulated using a standard Tucker-Barnes-Chakraborty (TBS) model, given the experimental parameters of tube voltage, tube current, Al filtration, and the distance from the origin of the X-rays to the detector. The accuracy of the simulated spectrum has been verified by comparing the half-value layer (HVL) of aluminium between simulated and experimentally measured spectra.

The simulated spectrum has a corresponding fluence (photons per unit area per unit energy) ($N(E_i)$). This fluence is used to calculate the portion of photons absorbed by the a-PbO layer ($N_{abs}(E_i)$) given by the Beer-Lambert law:

$$N_{abs}(E_i) = N(E_i)(1 - exp[-\alpha(E_i)\rho L_{PbO}]). \tag{B.3}$$

In equation A.3, $\alpha(E_i)$ is the mass attenuation coefficient, as a function of energy, ρ is the density, and L_{PbO} is the thickness, all pertaining to a-PbO.

E_{abs} is then calculated assuming that the fraction of energy absorbed is proportional to mass-energy coefficient ($\alpha_{en}(E_i)$) of a-PbO to $\alpha(E_i)$ ratio. The mass and mass-energy coefficients of PbO were obtained by summating the elemental coefficients for Pb and O from the NIST database [62]. Therefore E_{abs} is given as:

$$E_{abs} = AX \sum_i \left(\frac{\alpha_{en}(E_i)}{\alpha(E_i)} N_{abs}(E_i) E_i \right), \tag{B.4}$$

where A is the detector's effective area and X is incident exposure of the X-ray beam on the detectors surface. A is the area of the smallest electrode on the detector, which is the Au contact in this investigation. X was experimentally measured prior to XPM, with an ionization chamber placed where the detector sits. A blank ITO-coated glass substrate with a 1.1 µm thick PI layer was placed in front of the X-ray tube during exposure measurements to account for the attenuation of the substate and blocking layer.

References:

[1] K. Wang, H. Ou, and J. Chen, "Dual-gate photosensitive thin-film transistor-based active pixel sensor for indirect-conversion x-ray imaging," *IEEE Trans. Electron Devices*, vol. 62, no. 9, pp. 2894–2899, Sep. 2015, doi: 10.1109/TED.2015.2457449.

[2] S. Kasap *et al.*, "Amorphous and Polycrystalline Photoconductors for Direct Conversion Flat Panel X-Ray Image Sensors," *Sensors*, vol. 11, no. 5, pp. 5112–5157, May 2011, doi: 10.3390/s110505112.

[3] G. Zentai, "Comparison of CMOS and a-Si flat panel imagers for X-ray imaging," *2011 IEEE Int. Conf. Imaging Syst. Tech. IST 2011 - Proc.*, pp. 194–200, 2011, doi: 10.1109/IST.2011.5962217.

[4] J. Rowlands and J. Yorkston, "Flat Panel Detectors for Digital Radiography," in *Handbook of Medical Imaging*, vol. Vol 1., J. Beutel, H. Kundel, and R. Van Metter, Eds. Bellingham, Washington USA: SPIE Press, 2000, pp. 223–313.

[5] B. K. Cha *et al.*, "A pixelated CsI (Tl) scintillator for CMOS-based X-ray image sensor," *IEEE Nucl. Sci. Symp. Conf. Rec.*, vol. 2, pp. 1139–1143, 2006, doi:

10.1109/NSSMIC.2006.356046.

[6] M. Z. Kabir and S. Kasap, “Photoconductors for x-ray image detectors,” in *Springer Handbook of Electronic Photonics*, Springer, 2017, pp. 1125–1147.

[7] O. Semeniuk, O. Grynko, G. Juska, and A. Reznik, “Amorphous lead oxide (a-PbO): Suppression of signal lag via engineering of the layer structure,” *Sci. Rep.*, vol. 7, no. 1, pp. 1–7, 2017, doi: 10.1038/s41598-017-13697-2.

[8] G. Zentai, “Photoconductor-based (direct) large-area x-ray imagers,” *J. Soc. Inf. Disp.*, vol. 17, no. 6, p. 543, 2009, doi: 10.1889/jsid17.6.543.

[9] G. Zentai, L. Partain, M. Richmond, K. Ogusu, and S. Yamada, “50 μm pixel size a-Se mammography imager with high DQE and increased temperature resistance,” in *SPIE Physics of Medical Imaging*, 2010, vol. 7622, p. 762215, doi: 10.1117/12.845385.

[10] B. Zhao and W. Zhao, “Imaging performance of an amorphous selenium digital mammography detector in a breast tomosynthesis system,” *Med. Phys.*, vol. 35, no. 5, pp. 1978–1987, 2008, doi: 10.1118/1.2903425.

[11] J. G. Yorker, L. S. Jeromin, D. L. Y. Lee, E. F. Palecki, K. P. Golden, and Z. Jing, “Characterization of a full field digital mammography detector based on direct x-ray conversion in selenium,” *SPIE Phys. Med. Imaging*, vol. 4682, no. 203, pp. 21–29, 2002, doi: 10.1117/12.465568.

[12] O. Grynko, T. Thibault, E. Pineau, and A. Reznik, “The X-ray sensitivity of an amorphous lead oxide photoconductor,” *Sensors*, vol. 21, no. 21, Nov. 2021, doi: 10.3390/S21217321.

[13] O. Grynko, T. Thibault, E. Pineau, G. Juska, and A. Reznik, “Bilayer lead oxide X - ray

photoconductor for lag - free operation," *Sci. Rep.*, pp. 1–9, 2020, doi: 10.1038/s41598-020-77050-w.

[14] O. Grynko, E. Pineau, T. Thibault, G. DeCrescenzo, and A. Reznik, "Multilayer Amorphous Lead Oxide-based X-ray Detector," in *Proceedings of the 7th International Conference on Sensors and Electronic Instrumentation Advances (SEIA' 2021)*, 2021, no. 7, pp. 78–82.

[15] O. Semeniuk, A. Reznik, and V. Sukhovatkin, "Amorphous lead oxide based energy detection devices and methods of manufacture thereof," U.S. Patent 10,163,970, 2018.

[16] O. Semeniuk, "Lead Oxide (PbO) for direct conversion fluoroscopic detectors," Lakehead University, 2017.

[17] M. Simon *et al.*, "PbO as direct conversion x-ray detector material," *Med. Imaging 2004 Phys. Med. Imaging*, vol. 5368, no. May 2004, p. 188, 2004, doi: 10.1117/12.533010.

[18] O. Semeniuk, O. Grynko, G. Decrescenzo, G. Juska, K. Wang, and A. Reznik, "Characterization of polycrystalline lead oxide for application in direct conversion X-ray detectors," *Sci. Rep.*, vol. 7, no. 1, pp. 1–10, 2017, doi: 10.1038/s41598-017-09168-3.

[19] O. Semeniuk, A. Csik, S. Kökényesi, and A. Reznik, "Ion-assisted deposition of amorphous PbO layers," *J. Mater. Sci.*, vol. 52, no. 13, pp. 7937–7946, Jul. 2017, doi: 10.1007/s10853-017-0998-5.

[20] N. F. (Nevill F. Mott and E. A. (Edward A. Davis, *Electronic processes in non-crystalline materials*, 2d ed. New York: Clarendon Press ; Oxford University Press, 1979.

[21] S. Baranovski and O. Rubel, "Description of Charge Transport in Amorphous Semiconductors," in *Charge Transport in Disordered Solids with Application in*

Electronics, S. Baranovskii, Ed. John Wiley & Sons, Ltd, 2006, pp. 46–93.

[22] A. V. Nenashev *et al.*, "Field-enhanced mobility in the multiple-trapping regime," *Phys. Rev. B*, vol. 98, no. 3, Jul. 2018, doi: 10.1103/PhysRevB.98.035201.

[23] S. K. Mendis *et al.*, "CMOS active pixel image sensors for highly integrated imaging systems," *IEEE J. Solid-State Circuits*, vol. 32, no. 2, pp. 187–196, Feb. 1997, doi: 10.1109/4.551910.

[24] W. H. Maes, I. M. Peters, C. Smit, Y. Kessener, and J. Bosiers, "Low-dose performance of wafer-scale CMOS-based X-ray detectors," *Med. Imaging 2015 Phys. Med. Imaging*, vol. 9412, no. 1, p. 94120C, 2015, doi: 10.1117/12.2081996.

[25] M. Koniczek, L. Antonuk, Y. El-Mohri, A. Liang, and Q. Zhao, "Theoretical Investigation of the Noise Performance of Active Pixel Imaging Arrays Based on Polycrystalline Silicon Thin Film Transistors," *Int. J. Med. Phys. Res. Pract.*, vol. 44, no. 7, pp. 3491–3503, 2017, doi: 10.1002/mp.12257.

[26] O. Grynko, T. Thibault, E. Pineau, and A. Reznik, "Engineering of a Blocking Layer Structure for Low-Lag Operation of the a-PbO-Based X-Ray Detector," *IEEE Trans. Electron Devices*, vol. 68, no. 5, pp. 2335–2341, 2021, doi: 10.1109/TED.2021.3067616.

[27] S. M. SZE and K. N. Kwok, "Metal-Semiconductor Contacts," in *Physics of Semiconductor Devices*, 3rd ed., John Wiley and Sons, Inc., 2007, pp. 134–190.

[28] S. O. Kasap, "Semiconductors," in *Principles of Electronic Materials and Devices*, 4th ed., 2018, pp. 411–511.

[29] K. Chi Kao, "Charge Carrier Injection from Electrical Contacts," in *Dielectric Phenomena*

In Solids With Emphasis on Physical Concepts of Electronic Processes, 2004, pp. 327–378.

[30] S. A. Mahmood, M. Z. Kabir, O. Tousignant, H. Mani, J. Greenspan, and P. Botka, “Dark current in multilayer amorphous selenium x-ray imaging detectors,” *Appl. Phys. Lett.*, vol. 92, no. 22, 2008, doi: 10.1063/1.2938888.

[31] J. B. Frey, G. Belev, O. Tousignant, H. Mani, L. Laperriere, and S. O. Kasap, “Dark current in multilayer stabilized amorphous selenium based photoconductive x-ray detectors,” *J. Appl. Phys.*, vol. 112, no. 1, pp. 1–10, 2012, doi: 10.1063/1.4730135.

[32] S. A. Mahmood and M. Z. Kabir, “Dark current mechanisms in stabilized amorphous selenium based n-i detectors for x-ray imaging applications,” *J. Vac. Sci. Technol. A Vacuum, Surfaces, Film.*, vol. 29, no. 3, p. 031603, 2011, doi: 10.1116/1.3580902.

[33] M. Z. Kabir and S. Al Imam, “Determination of deep trapping states of the hole blocking layer in multilayer amorphous selenium X-ray detectors using transient dark current analysis,” *Can. J. Phys.*, vol. 92, no. 7–8, pp. 641–644, 2014, doi: 10.1139/cjp-2013-0536.

[34] G. S. Belev, “Electrical Properties of Amorphous Selenium Based Photoconductive Devices for Application in X-Ray Image Detectors,” University of Saskatchewan, 2007.

[35] I. Dash, “Preparation & Characterization of n-Type Amorphous Se Films as Blocking Layers in a-Se X-ray Detectors,” University of Saskatchewan, 2009.

[36] S. Abbaszadeh, N. Allec, S. Ghanbarzadeh, U. Shafique, and K. S. Karim, “Investigation of hole-blocking contacts for high-conversion-gain amorphous selenium detectors for X-ray imaging,” *IEEE Trans. Electron Devices*, vol. 59, no. 9, pp. 2383–2389, 2012, doi: 10.1109/TED.2012.2204998.

[37] K. Kikuchi *et al.*, “Hole-blocking mechanism in high-gain avalanche rushing amorphous photoconductor (HARP) film,” *Phys. Status Solidi Curr. Top. Solid State Phys.*, vol. 8, no. 9, pp. 2800–2803, Sep. 2011, doi: 10.1002/PSSC.201084055.

[38] O. Bubon, “Amorphous selenium (a-Se) avalanche photodetector for applications in Positron Emission Tomography (PET),” Lakehead University, 2011.

[39] M. Z. Kabir and S. Al Imam, “Transient and steady-state dark current mechanisms in amorphous selenium avalanche radiation detectors,” *Appl. Phys. Lett.*, vol. 102, no. 15, 2013, doi: 10.1063/1.4802840.

[40] J. Duan *et al.*, “TiO2/ZnO/TiO2 sandwich multi-layer films as a hole-blocking layer for efficient perovskite solar cells,” *Energy Res.*, vol. 40, pp. 806–813, 2016, doi: 10.1002/er.

[41] S. Abbaszadeh, “Indirect conversion amorphous selenium photodetectors for medical imaging applications,” Waterloo University, 2014.

[42] A. Reznik *et al.*, “Avalanche multiplication in amorphous selenium and its utilization in imaging,” *J. Non. Cryst. Solids*, vol. 354, no. 19–25, pp. 2691–2696, 2008, doi: 10.1016/j.jnoncrysol.2007.09.058.

[43] A. Camlica, M. Z. Kabir, J. Liang, P. M. Levine, D. L. Lee, and K. S. Karim, “Use of Pulse-Height Spectroscopy to Characterize the Hole Conduction Mechanism of a Polyimide Blocking Layer Used in Amorphous-Selenium Radiation Detectors,” *IEEE Trans. Electron Devices*, vol. 67, no. 2, pp. 633–639, 2020, doi: 10.1109/TED.2019.2958789.

[44] H. Huang and S. Abbaszadeh, “Recent Developments of Amorphous Selenium-Based X-Ray Detectors: A Review,” *IEEE Sens. J.*, vol. 20, no. 4, pp. 1694–1704, 2020, doi:

10.1109/JSEN.2019.2950319.

[45] D. J. Liaw, K. L. Wang, Y. C. Huang, K. R. Lee, J. Y. Lai, and C. S. Ha, "Advanced polyimide materials: Syntheses, physical properties and applications," *Prog. Polym. Sci.*, vol. 37, no. 7, pp. 907–974, 2012, doi: 10.1016/j.progpolymsci.2012.02.005.

[46] H. MicroSystems, "PI-2600 Series – Low Stress Applications," 2009.

[47] S. C. Systems, "SCS Parylene Properties - High Performance Conformal Coatings." Specialty Coating Systems, Indianapolis, IN, 2018.

[48] S. Abbaszadeh, C. C. Scott, O. Bubon, A. Reznik, and K. S. Karim, "Enhanced detection efficiency of direct conversion x-ray detector using polyimide as hole-blocking layer," *Sci. Rep.*, vol. 3, pp. 1–7, Nov. 2013, doi: 10.1038/srep03360.

[49] O. Semeniuk, G. Juska, J. O. Oelerich, M. Wiemer, S. D. Baranovskii, and A. Reznik, "Charge transport mechanism in lead oxide revealed by CELIV technique," *Sci. Rep.*, vol. 6, no. 1, pp. 1–9, 2016, doi: 10.1038/srep33359.

[50] O. Semeniuk, G. Juska, J. O. Oelerich, K. Jandieri, S. D. Baranovskii, and A. Reznik, "Transport of electrons in lead oxide studied by CELIV technique," *J. Phys. D. Appl. Phys.*, vol. 50, no. 3, p. 035103, Jan. 2017, doi: 10.1088/1361-6463/50/3/035103.

[51] V. Loustauneau *et al.*, "Imaging performance of a clinical selenium flat-panel detector for advanced applications in full-field digital mammography," *Med. Imaging 2003 Phys. Med. Imaging*, vol. 5030, no. 514, p. 1010, 2003, doi: 10.1117/12.484075.

[52] O. Semeniuk, A. Reznik, and V. Sukhovatkin, "Amorphous Lead Oxide based energy detection devices and methods of manufacture," US 10,163,970 B2, 2018.

[53] J. Bushberg, A. Seibert, E. Leidholdt, and J. Boone, *The Essential Physics for Medical Imaging*, 2nd ed. Philadelphia, PA: Lippincott Williams and Wilkins, 2002.

[54] M. Simon *et al.*, “Analysis of lead oxide (PbO) layers for direct conversion X-ray detection,” *IEEE Trans. Nucl. Sci.*, vol. 52, no. 5 III, pp. 2035–2040, 2005, doi: 10.1109/TNS.2005.856790.

[55] D. Min, S. Li, M. Cho, and A. R. Khan, “Investigation into surface potential decay of polyimide by unipolar charge transport model,” *IEEE Trans. Plasma Sci.*, vol. 41, no. 12, pp. 3349–3358, 2013, doi: 10.1109/TPS.2013.2270377.

[56] K. Koughia, Z. Shakoor, S. O. Kasap, and J. M. Marshall, “Density of localized electronic sates in a-Se from electron time-of-flight photocurrent measurements,” *J. Appl. Phys.*, vol. 97, no. 3, 2005, doi: 10.1063/1.1835560.

[57] A. V. Nenashev *et al.*, “Release of carriers from traps enhanced by hopping,” *Phys. Rev. B*, vol. 98, no. 155207, pp. 1–9, Oct. 2018, doi: 10.1103/PhysRevB.98.155207.

[58] A. Qamar *et al.*, “X-ray spectroscopic study of amorphous and polycrystalline PbO films, α-PbO, and β-PbO for direct conversion imaging,” *Sci. Rep.*, vol. 7, no. 1, pp. 1–10, 2017, doi: 10.1038/s41598-017-13703-7.

[59] A. Qamar, M. Ruhul Amin, O. Grynko, O. Semeniuk, A. Reznik, and A. Moewes, “A Probe of Valence and Conduction Band Electronic Structure of Lead Oxide Films for Photodetectors,” *ChemPhysChem*, vol. 20, no. 24, pp. 3328–3335, 2019, doi: 10.1002/cphc.201900726.

[60] S. O. Kasap and J. A. Rowlands, “Direct-conversion flat-panel X-ray image detectors,” *IEE*

Proc. Circuits, Devices Syst., vol. 149, no. 2, pp. 85–96, Apr. 2002, doi: 10.1049/IP-CDS:20020350.

[61] S. Abbaszadeh, S. Ghaffarii, S. Siddiquee, M. Z. Kabir, and S. K. Karim, “Characterization of Lag Signal in Amorphous Selenium Detectors,” *IEEE Trans. Electron Devices*, vol. 63, no. 2, pp. 1–6, 2016.

[62] J. H. Hubbell and S. M. Seltzer, “Table of X-Ray Mass Attenuation Coefficients and Mass Energy-Absorption Coefficients from 1 keV to 20 MeV for Elements Z = 1 to 92 and 48 Additional Substances of Dosimetric Interest.,” 2004. [Online]. Available: https://www.nist.gov/pml/x-ray-mass-attenuation-coefficients. [Accessed: 06-Jul-2022].